Editors' Suggestion

Transport of inertial ellipsoidal particles in turbulent flow over rough walls

D. Saccone, M. De Marchis,* and B. Milici†
Facoltà di Ingegneria e Architettura, Università di Enna Kore, 94100 Enna EN, Italy

C. Marchioli‡
Dipartimento Politecnico di Ingegneria e Architettura,
Università di Udine and Dipartimento di Fluidodinamica, CISM di Udine, 33100 Udine UD, Italy

(Received 9 November 2022; accepted 6 July 2023; published 16 August 2023)

The dispersion of rigid elongated particles in turbulent channel flow bounded by rough walls is examined. In particular, the interplay between particle inertia, particle length, and wall roughness characteristics in determining particle spatial distribution, preferential orientation, and alignment within the flow is analyzed. The dispersion process is investigated by performing direct numerical simulations of the turbulent flow coupled with the Lagrangian tracking of the particles, modeled as prolate ellipsoids with varying aspect ratio and inertia, under dilute flow conditions. Simulations are carried out at friction Reynolds number $\mathrm{Re}_\tau = 180$ based on the channel half height in a domain confined by walls with different two-dimensional roughness characteristics. Particle elongation is varied considering different aspect ratios (ranging from $\lambda = 1$ for the reference case of spherical particles to $\lambda = 10$ for the longest particle set) while particle inertia is varied considering different Stokes numbers (ranging from $\mathrm{St}^+ = 1$ for the least inertial particles to $\mathrm{St}^+ = 100$ for the most inertial ones), for a total of 12 different particle sets. Our results show that particles are affected by the turbulent structures that form near the rough walls in a way that is biased both by elongation, namely length, and inertia. This is not observed with smooth walls: In this case, increasing particle inertia always leads to a stronger turbophoretic particle drift to the walls. Elongation is observed to have a quantitative effect on the slip velocity statistics, particularly for particles with small Stokes number. Differences induced by a change of the aspect ratio tend to vanish as particle inertia increases, since the relative translational motion between the particles and the surrounding fluid appears to be closely connected to preferential concentration phenomena. Wall roughness modifies the overall dynamics of the particles, as well as their distribution, orientation, and alignment with flow direction, especially in the near-wall region. Roughness hinders long-term wall deposition of particles and determines a more uniform spatial distribution across the channel. In the near-wall region, elongated particles tend to align with the streamwise direction even in the presence of large-scale roughness, albeit to a lesser extent compared to the case of smooth walls. A stronger effect of roughness is noticed on the alignment along the spanwise and wall-normal directions. Such alignment, as well as preferential orientation, is hampered by the strong velocity fluctuations induced by roughness and the behavior of the ellipsoidal particles resembles again that of spherical particles.

DOI: 10.1103/PhysRevFluids.8.084303

*mauro.demarchis@unikore.it
†barbara.milici@unikore.it
‡marchioli@uniud.it

I. INTRODUCTION

Understanding the dynamics of inertial particles in turbulent flows is of paramount importance for the successful design of industrial operations, but also for improving the knowledge of many natural phenomena. Indeed, the processes of transport, deposition, and resuspension of inertial particles are encountered in a wide variety of applications, ranging from pulp and paper production [1] and combustion processes [2,3] to atmospheric dispersion of aerosols [4,5], cloud microphysics [6,7], sediment transport [8,9], and pollution control [10,11], to name a few. In many of these applications, the carrier flow is turbulent and bounded by regular or irregular walls, which play a role in determining the macroscopic features of particle transport, e.g., particle transfer toward and away from the wall and particle-wall interaction [12].

To improve the knowledge of wall-bounded turbulent dispersed flows, numerous studies have been conducted over the past decades. The majority of these studies, which include both laboratory experiments (see Refs. [13–16] among the most recent ones), and numerical simulations (see Refs. [17–23] among others) considered flow domains bounded by smooth walls and laden with particles having different inertia and shapes. The reader is also referred to the recent review by Ref. [24] for a more complete survey on spherical particles in homogeneous and canonical wall-bounded flows. The role of particle inertia in determining how the particles follow the flow and how they are transported in the wall-normal direction has been studied mainly in the limit of pointwise, spherical particles [22,25,26]. Assuming spherical particles is very convenient because of several factors: Perfect spheres are simple to model, their behavior is well known, and lastly there are many available of models in the literature to describe the particle–fluid interactions [27]. Having fixed the particle shape, inertia can be modified by changing the particle size and/or the specific density, given by the ratio of the particle density to the fluid density. In the point-particle limit, however, the size must be kept smaller than the Kolmogorov length scale of the flow: Therefore, it is more convenient to vary particle inertia via the specific density. By doing so, it was possible to demonstrate that lighter particles, which would need entrainment in a strongly coherent structure to continue their journey toward the wall, may lose more quickly their momentum due to the decrease in the sweep intensity in the viscous sub-layer. However, heavy particles are able to leave the coherent sweep and move toward the wall in free-flight more easily due to their high inertia [28,29]. Overall, heavy spherical particles are found to accumulate and then segregate near the walls when these are smooth [17,30,31]. This tendency is generally attributed to turbophoresis [32–34], which produces a wallward drift that seems to be independent of the large-scale outer motions of the flow [20].

It is clear that modeling particles as perfect spheres may be inaccurate, if not unrealistic, for the many applications of practical interest in which the dispersed phase is represented by nonspherical particles [35]. In spite of this, turbulent flows laden with nonspherical particles have received comparatively less attention until the last decade, when the tremendous advances of measurement and simulation capabilities have made it possible to handle the computational costs and the mathematical complexities associated to the modeling of nonspherical particle motion in a fluid flow. First off, these complexities arise from the strong coupling that exists between the translation and the rotation of a nonspherical particle. In addition, a wider set of geometrical parameters must be taken into account: While a sphere has just one characteristic length scale (its diameter), even the simplest type of nonspherical particle, e.g., a disk, a cylinder, or an ellipsoid, is uniquely defined by at least two characteristic length scales. Among numerical works, which are more relevant in the frame of the present study, the first contributions paving the way to the study of nonspherical particles in fluid flows was given by Ref. [36] and later by Ref. [37]. Following the pioneering theoretical and analytical analyses of Refs. [38–41], these studies exploited Lagrangian tracking to investigate the combined actions of rotation, inertia and gravity on the velocity of prolate and oblate spheroids settling in a synthetic cellular flow. These studies aroused interest from the scientific community and were later followed by experimental and numerical works aimed at improving the knowledge of the physical processes that govern the dispersion of elongated inertial particles (both rigid and flexible) in a turbulent suspension [15,16,21,42–48].

Most of the available numerical works focus on the case of ellipsoidal particles, namely prolate or oblate spheroids with regular axisymmetric shape and a single aspect ratio, referred to as λ hereinafter and defined as the ratio between the semi major axis and the semi minor axis of the ellipsoid. These works (see, for instance, Refs. [49,50] and references therein) have shown that, when the ellipsoidal particles are small compared to the Kolmogorov scale of the flow, their behavior is similar to that of the spherical particles [17,43]: These elongated particles are still transferred by sweeps in the near-wall region, where they preferentially accumulate in the low-speed streaks, and must be entrained in ejections to be transported from the wall region back to the outer flow. The transport mechanisms is biased only from a quantitative point of view by elongation, which is found to have an effect on the slip velocity statistics, particularly for ellipsoids with small Stokes [51]. As the Stokes number increases, however, differences induced by a change of elongation, namely aspect ratio, tend to vanish and particle behavior is dominated by inertia [21]. Besides particle transport mechanisms, which are connected to particle translational dynamics, studies dealing with nonspherical particles have shed light also on the rotational dynamics, which determine the preferential orientation attained by the particles. It was shown by Refs. [49,50,52] that ellipsoidal particles preferentially orient themselves along the streamwise flow direction when they are in the viscous region, as also confirmed later by Refs. [53–55]. Other studies on orientation highlighted the different particle rotation patterns that can be observed at the channel center compared to the near-wall region [56]. In the outer region, prolate ellipsoidal particles rotate around their symmetry axis; near the wall, however, they are forced by shear to rotate normal to their symmetry axis. Similar results are reported by Ref. [57] on their analysis on bed-load transport of nonspherical sediments in open channel flow. We remark here that preferential orientation is a crucial phenomenon also because it affects particle acceleration. As shown by Ref. [58], the acceleration of an ellipsoidal particle is directly related to the net force the particle experiences along its trajectory. In turn, this aerodynamic force depends not only on particle shape but also on particle orientation relative to the flow.

Besides the specific type of particles that one may consider, another important feature of wall-bounded turbulent dispersed flows is the type of bounding walls, which may exhibit a textured surface with different degrees of topographical complexity or simply surface defects and irregularities due to natural erosion, manufacturing process and working damage [59,60]. The simplest case, which is by far the most widely studied in the literature, is represented by hydrodynamically smooth walls that have no texture or defects and do not interact with near-wall turbulence. However, most engineered surfaces are not smooth. Rather, they are characterized by a certain roughness that is known to have an important effect on the flow in the wall-dominated region (i.e., inner wall region and turbulent zone). The need to understand the physical mechanisms by which the presence of wall roughness modifies the flow, has stimulated numerous experimental and numerical analyses (see Refs. [61–65] and references therein, among others). Studies have been conducted considering both pipes and channels flow [66–69], to gain knowledge of the flow interaction with rough surfaces and to find a universal parameter through which roughness effects on fluid velocity field could be predicted. A comprehensive review was recently published by Ref. [70] to highlight the state of art and to encourage future analyzes on this topic, which has not yet been fully understood. Nevertheless, the most important effect on the flow field appears to be represented by the lowering of the mean velocity profile, referred to as Roughness Function ΔU^+ [71–73] and the increase of the flow turbulence intensity. Clearly, this latter effect has an impact also on particle translation and rotation within the flow. Such an impact has been studied almost exclusively for the case of spherical particles, showing that roughness leads to an increase of particle-wall collisions [74] and to a different spatial distribution of the particles throughout the flow domain as compared to the smooth-wall case [75]. Indeed, particles in flow domains with rough bounding walls tend to accumulate away from the wall, rather than within the viscous layer, and consequently populate the center of the channel. This attenuation of the particle trapping in the viscous sub-layer and the consequent increased dispersion in the outer region have been demonstrated by several (albeit not many) experimental and numerical studies focused on the transport of spherical heavy particles in domains bounded by regular or irregular rough walls [76–80], but also in a spatially developing turbulent boundary layer over a hemisphere-roughened wall [81]. Recently, the authors of Ref. [82] were able to show that particles transport and deposition within rough walls can be categorized into three distinct regimes dictated by the Stokes number. This finding, obtained performing a direct numerical simulation of a turbulent pipe flow at fixed friction Reynolds number and changing the roughness size, suggests that the behavior of small spherical particles can still be parameterized solely by their inertia. Whether this parametrization works also for nonspherical particles remains an open question, which we will try to address in this paper.

We made a first effort in this direction in a recent work [83], in which we performed a series of direct numerical simulations to evaluate the effect that hydrodynamically rough walls have on the turbulent dispersion of rigid fibers. In particular, the study examined the deposition and resuspension of fibers with fixed inertia (namely, fixed Stokes number, $\mathrm{St}^+ = 5$) but different length (namely, different aspect ratio, $\lambda = 1,\ 3,\ 10$) in a channel bounded by two-dimensional roughness. Three different roughness configurations were examined, showing that roughness effects are dominant in the fiber dispersion process, whereas length effects play a role mainly in determining the mean orientation of the fibers. The results confirmed that in rough wall conditions the dynamics of nonspherical particles is substantially different from what one observes in the smooth wall case. However, the specific role of particle inertia and its interplay with particle elongation and with the topographical complexities associated with roughness could not be explored. This is precisely the objective of this paper, which is organized as follows: in Sec. II we introduce the numerical methodology, the flow domain and particle characteristics; results are presented and discussed in Sec. III; finally, the concluding remarks are provided in Sec. IV.

II. METHODOLOGY

We consider a turbulent Poiseuille flow of an incompressible Newtonian fluid in a channel bounded by two rough walls, performing direct numerical simulations of the continuity and Navier–Stokes equations, coupled with a Lagrangian approach to compute the particle trajectories. The governing equations in dimensionless scalar form read as

$$\frac{\partial u_i}{\partial x_i} = 0, \tag{1}$$

$$\frac{\partial u_i}{\partial t} + \frac{\partial u_i u_j}{\partial x_j} - \frac{1}{Re_\tau}\frac{\partial^2 u_i}{\partial x_j \partial x_j} + \frac{\partial p}{\partial x_i} + \Pi \delta_{i1} = 0, \tag{2}$$

where u_i is the ith fluid velocity component, x_i is the ith coordinate, p is the kinematic pressure, Π is the imposed mean pressure gradient that drives the flow, δ_{i1} is the Kronecker δ function and $\mathrm{Re}_\tau = u_\tau \delta/\nu = 180$, is the friction Reynolds number, based on the friction velocity u_τ, the channel half-height δ and the fluid kinematic viscosity ν. Note that this value is slightly higher than that reported by Ref. [83], namely $\mathrm{Re}_\tau = 150$. Simulations were carried out using the modified version of 3D numerical model PANORMUS (parallel numerical open-source model for unsteady flow simulation) and considering air with density $\rho = 1.3\ \mathrm{kg/m^3}$ and kinematic viscosity $\nu = 15.7 \times 10^{-}6\ \mathrm{m^2/s}$, which yields $u_\tau = 0.14\ \mathrm{m/s}$ in a 4-cm-high channel. The PANORMUS code is second-order accurate both in time and space and exploits an explicit Adams-Bashforth method for the time advancement of the solution. A fractional-step technique is used to overcome the pressure-velocity decoupling that is typical of incompressible flows. More details on the code can be found in Ref. [84]. The numerical code has been successfully validated in industrial fields [85] as well as in environmental flow applications [86,87].

The particles are modeled as prolate ellipsoids with aspect ratio $\lambda = b/a$, where a is the semiminor axis and b is the semimajor axis of the ellipsoid. The equation describing the translational

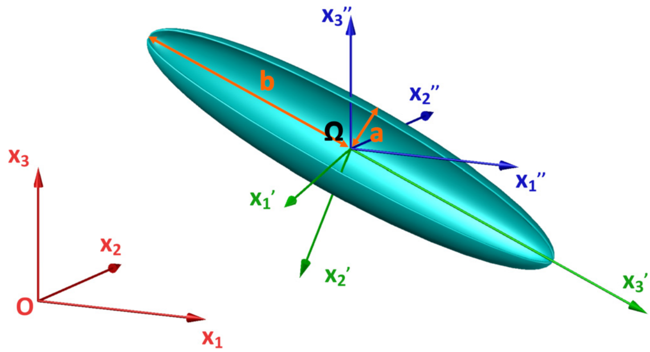

FIG. 1. Reference frames used to describe the motion of an ellipsoidal particle.

motion of an individual particle, written in vector form, reads as follows:

$$\frac{d\mathbf{v}_p}{dt} = \frac{\mathbf{F}}{m_p}, \tag{3}$$

where $\mathbf{v}_p$ is the particle velocity, $\mathbf{F}$ is the hydrodynamic drag force acting on the particle, and $m_p = (4/3)\pi a^3 \lambda \rho_p$ is the mass of the particle, with ρ_p its density. The drag force $\mathbf{F}$ is expressed as follows [39]:

$$\mathbf{F} = \mu\, \mathbf{K}\, (\mathbf{u}_{@p} - \mathbf{v}_p), \tag{4}$$

where μ is the fluid dynamic viscosity, $\mathbf{K}$ is the resistance tensor, and $\mathbf{u}_{@p}$ is the fluid velocity at the particle position. Note that this expression is strictly valid for an ellipsoid under creeping flow conditions, which require the particle Reynolds number, defined here as $\mathrm{Re}_p = 2a(\mathbf{u}_{@p} - \mathbf{v}_p)/\nu$, to be much smaller than unity. In the simulations with flat walls, such condition is met for all particle sets outside of the buffer layer, but values may become of the order of unity in the near-wall region for the particles with larger inertia. In the simulations with rough walls, the $\mathrm{Re}_p \ll 1$ is met only for the $\mathrm{St}^+ = 1$ and $\mathrm{St}^+ = 5$ particle sets outside of the buffer layer, and large values, up to $\mathrm{Re}_p \simeq 5$, can be reached in the near-wall region. This implies that the drag force formulation given by Eq. (4) may become inaccurate in some regions of the flow and corrections would be needed. Even though several correction formulas exist to account for finite-Reynolds-number effects on the motion of spherical particles, no such suitably validated corrections (e.g., Schiller-Naumann-like corrections) yet exist for nonspherical particles in turbulence, as also discussed in Ref. [21] and more recently in the review by Ref. [88]. As far as our knowledge goes, correlations for finite-size ellipsoids have been developed only for simple flows (e.g., steady and unbounded uniform flow as in Refs. [89–91] or wall-bounded linear shear flow as in Refs. [92,93]) and typically at particle Reynolds numbers much higher than those considered in our study. As recently pointed out by Ref. [88], the existing correlations for the drag coefficients are still laden with high uncertainty, which propagates in the numerical results. In view of this uncertainty, and also considering the need to provide a direct comparison with similar studies in channel flow with sooth walls, e.g., Refs. [15,83], we decided not to include such corrections. Nevertheless, development of finite-Reynolds-number corrections for the drag force, but also for the torque acting from the viscous fluid on ellipsoidal particles, is indeed welcome as it would make the Lagrangian particle modeling way more versatile. In rough conditions, developing such models can be further complex, as suggested by the recent findings of Ref. [92].

The resistance tensor $\mathbf{K}$ is expressed with respect to the Eulerian (inertial) frame of reference, $\mathbf{x} = \langle x_1, x_2, x_3 \rangle$, shown in Fig. 1 together with the other frames of reference that are used to describe the motion of the particle: The Lagrangian particle frame, $\mathbf{x}' = \langle x'_1, x'_2, x'_3 \rangle$, which is attached to the particle and has its origin located at the center of mass of the particle; and the comoving frame,

$\mathbf{x}'' = \langle x_1'', x_2'', x_3'' \rangle$, which also has its origin at the center of mass of the particle but keeps its axes parallel to those of the inertial frame. Given these frames, the resistance tensor is computed as $\mathbf{K} = \mathbf{A}^t\mathbf{K}'\mathbf{A}$, where $\mathbf{K}'$ is computed in the particle frame, $\mathbf{A}$ is the orthogonal transformation matrix comprising the direction cosines, and $\mathbf{A}^t$ is its transpose. Upon matching the axes of the particle frame with the principal axes of resistance, the diagonal form of **K**' can be computed as

$$\mathbf{K}' = \begin{bmatrix} k_{x_1'x_1'} & 0 & 0 \\ 0 & k_{x_2'x_2'} & 0 \\ 0 & 0 & k_{x_3'x_3'} \end{bmatrix}, \tag{5}$$

where the diagonal elements are defined as follows:

$$k_{x_1'x_1'} = k_{x_2'x_2'} = \frac{16(\lambda^2-1)^{3/2}}{[(2\lambda^2-3)\cdot\ln(\lambda+\sqrt{\lambda^2-1}]+\lambda\sqrt{\lambda^2-1}}, \tag{6}$$

$$k_{x_3'x_3'} = \frac{8(\lambda^2-1)^{3/2}}{[(2\lambda^2-1)\cdot\ln(\lambda+\sqrt{\lambda^2-1}]+\lambda\sqrt{\lambda^2-1}}. \tag{7}$$

The lift force was not included in Eq. (3). The main reason being that the study of the lift on nonspherical particles is very limited compared to the literature available on the lift on spheres and, therefore, no reliable model for this force is available. There is no analytical treatment of the lift on a force-free fiber, neither is there any literature available for the hydrodynamic lift of a particle with high aspect ratio as a function of the distance from the wall in the presence of a turbulent flow. To the best of our knowledge, the only available study is the one by the authors of Ref. [94] for the case of shear flow. Gravity is also neglected. The main reason for this choice is to isolate the role of turbulence in determining the spatial distribution of the dispersed phase in isolation from other effects. This was also the objective of previous DNS-based studies dealing with fiber dispersion in turbulent channel flow over smooth walls (as, for instance, Refs. [23,49,50]), which represent the reference case that we consider to evaluate the interplay between the large-scale roughness of the walls and the inertia of the particles in isolation from other effects. To make a direct comparison of our results with those reported in the above-mentioned DNS-based studies, the neglect of gravity appears to be an inevitable choice. Nevertheless, the inclusion of gravity is definitely a future development of the present study, considering that it can influence the slip velocity by decorrelating particle velocity from the fluid velocity seen by the particles and hence gravitational settling (considered in previous studies for the case of rigid fibers transported by turbulence in a smooth-wall channel, see, e.g., Refs. [54,55]).

The rotational motion of the particles is given by the Euler equations, formulated in the particle frame:

$$I'_{x_1x_1}\frac{d\omega'_{x_1}}{dt} - \omega'_{x_2}\omega'_{x_3}\left(I'_{x_2x_2} - I'_{x_3x_3}\right) = N'_{x_1}, \tag{8}$$

$$I'_{x_2x_2}\frac{d\omega'_{x_2}}{dt} - \omega'_{x_3}\omega'_{x_1}\left(I'_{x_3x_3} - I'_{x_1x_1}\right) = N'_{x_2}, \tag{9}$$

$$I'_{x_3x_3}\frac{d\omega'_{x_3}}{dt} - \omega'_{x_1}\omega'_{x_2}\left(I'_{x_1x_1} - I'_{x_2x_2}\right) = N'_{x_3}, \tag{10}$$

where ω'_{x_1}, ω'_{x_2}, and ω'_{x_3} are the components of the angular velocity vector. The principal moments of inertia are

$$I'_{x_1x_1} = I'_{x_2x_2} = \frac{(1+\lambda^2)m_pa^2}{5} \quad I'_{x_3x_3} = \frac{2m_pa^2}{5}. \tag{11}$$

The torque components N'_{x_1}, N'_{x_2}, and N'_{x_3} were derived by Ref. [38] for an ellipsoid subjected to linear shear under creeping flow conditions. The effect of convective fluid inertia on the torque has been neglected. The main reason for this choice is that not much is known about the modeling of fluid inertia effects for the case of elongated particles. Most of the available studies focus on particles settling in a fluid at rest, which is a physical instance much simpler than the one considered here. Also, while the corrections to the translational motion, in particular for a sphere, are very well understood only for small-particle Reynolds numbers [7,95], the effect of fluid inertia upon the angular dynamics in the same regime has been less studied. Up to now, analytic expressions were proposed by Ref. [96] for nearly spherical particles, by Ref. [97] for slender bodies, and more recently by Ref. [98] for spheroids of arbitrary aspect ratios. All of these expressions, however, have not been validated experimentally yet: A first effort in this direction has been taken recently by Ref. [99]. Also missing is a well-established consensus on the conditions under which it may be justified to neglect fluid inertia for the translational and angular dynamics of nonspherical particles in turbulent flow at varying particle inertia and settling velocity: Only few recent studies are available, but these are focused on the settling of spheroids in unbounded turbulent or laminar flows. Recently [95] have proposed the ratio $\mathcal{R}$ between the magnitudes of the convective fluid-inertia torque and Jeffery's torque. In the slender body limit, the ratio R can be more simply expressed as [7,95]

$$\mathcal{R} = \frac{|\mathbf{u}_{@p} - \mathbf{v}_p|^2}{|\boldsymbol{\Omega} - \boldsymbol{\omega}|} = \frac{\mathrm{Re}_p^2}{\mathrm{Re}_s}, \tag{12}$$

where $|\mathbf{u}_{@p} - \mathbf{v}_p|$ is the absolute value of the particle-to-fluid relative velocity (translational slip velocity), $|\boldsymbol{\Omega} - \boldsymbol{\omega}|$ is the absolute value of the particle-to-fluid relative angular velocity (rotational slip velocity), and Re_s is the shear Reynolds number. Based on this definition, fluid inertia can be neglected when $R \ll 1$. In the flow configurations considered here, in which gravitational settling was neglected, it could be argued that the condition $R \ll 1$ can be met in the near-wall region, where the mean shear of the flow is strong and the slip velocity is comparatively small regardless of the Stokes number: Therefore, both the rotation and the orientation of the particles should be dominated by the flow shear, and the effect of the fluid-inertia torque should be negligible. To some extent, this is reassuring since the near-wall region is where particles interact more substantially with roughness. Away from the wall, however, the mean shear of the flow gradually vanishes and fluid inertia effects may become important, especially for the largest Stokes numbers we simulated. In this case, the assumptions made in our study may become inaccurate and it would indeed be very interesting to include the additional torque due to fluid inertia, which is expected to induce a preferential alignment of the particles (with its broad side relative to the streamwise direction rather than a random orientation).

We finally note that an increase of the aspect ratio λ determines an increase of the moments of inertia and, in turn, to a decrease of particle rotation for a given underlying flow field. At the same time, a larger λ corresponds to an increase of the diagonal elements of the resistance tensor, namely to an increase of the drag force for a given relative velocity between the particle and the surrounding fluid.

The complete set of equations considered to describe the translational and rotational motion of the particles, in dimensionless form, reads as [50]

$$\text{Kinematics}\begin{cases} \frac{d\mathbf{X}_{p,(G)}}{dt} = \mathbf{v}_p \\ \frac{de_0}{dt} = \frac{1}{2}\left(-e_1\omega_{x_1'} - e_2\omega_{x_2'} - e_3\omega_{x_3'}\right) \\ \frac{de_1}{dt} = \frac{1}{2}\left(e_0\omega_{x_1'} - e_3\omega_{x_2'} + e_2\omega_{x_3'}\right) \\ \frac{de_2}{dt} = \frac{1}{2}\left(e_3\omega_{x_1'} + e_0\omega_{x_2'} - e_1\omega_{x_3'}\right) \\ \frac{de_3}{dt} = \frac{1}{2}\left(-e_2\omega_{x_1'} + e_1\omega_{x_2'} + e_0\omega_{x_3'}\right) \end{cases}, \tag{13}$$

$$\text{Dynamics}\begin{cases} \frac{d\mathbf{v}_p}{dt} = \frac{3}{4\lambda Sa^2}\mathbf{K}\cdot(\mathbf{u}_p - \mathbf{v}_p) \\ \frac{d\omega_{x_1'}}{dt} = \omega_{x_2'}\omega_{x_3'}\left(1 - \frac{2}{1+\lambda^2}\right) + \frac{20[(1-\lambda^2)f' + (1+\lambda^2)(\xi' - \omega_{x_1'})]}{(\alpha_0+\lambda^2\gamma_0)(1+\lambda^2)Sa^2} \\ \frac{d\omega_{x_2'}}{dt} = \omega_{x_1'}\omega_{x_3'}\left(\frac{2}{1+\lambda^2} - 1\right) + \frac{20[(\lambda^2-1)g' + (\lambda^2+1)(\eta' - \omega_{x_2'})]}{(\alpha_0+\lambda^2\gamma_0)(1+\lambda^2)Sa^2} \\ \frac{d\omega_{x_3'}}{dt} = \frac{20}{(2\alpha_0)Sa^2}\left(\chi' - \omega_{x_3'}\right) \end{cases}, \tag{14}$$

TABLE I. Details of all cases: Re_τ is the friction Reynolds number, Lx_1, Lx_2, and Lx_3 are the domain sizes; Nx_1, Nx_2, and Nx_3 are the number of cells; Δx_1^+, Δx_2^+, $\Delta x_{3,\min}^+$, and $\Delta x_{3,\max}^+$ are the mesh resolutions (superscript $^+$ indicates nondimensional variables in wall units, obtained using the fluid kinematic viscosity ν and the friction velocity $u*$).

Case	Re_τ	Lx_1	Lx_2	Lx_3	Nx_1	Nx_2	Nx_3	Δx_1^+	Δx_2^+	$\Delta x_{3,\min}^+$	$\Delta x_{3,\max}^+$
F1	180	$2\pi\delta$	$\pi\delta$	2δ	128	128	128	8.8	4.4	0.12	7.1
R1	180	$4\pi\delta$	$\pi\delta$	2δ	256	128	128	8.8	4.4	0.06	7.7
R2	180	$4\pi\delta$	$\pi\delta$	2δ	256	128	128	8.8	4.4	0.06	7.7
R3	180	$4\pi\delta$	$\pi\delta$	2δ	256	128	128	8.8	4.4	0.06	7.7

where vector $\mathbf{x}_{p,(G)}$ provides the instantaneous position of the center of mass G of the ellipsoid, e_i are the Euler parameters, ω_{x_i} is the ith component of the ellipsoid's angular velocity, and S is the particle-to-fluid density ratio. The parameters α_0 and γ_0 were derived by Ref. [38] to compute the torque components for an ellipsoid subjected to linear shear under creeping flow conditions. The quantities f', g', ξ', η', and χ' are the elements of the fluid rate of strain tensor and fluid rotation tensor, all expressed in the particle frame. The equations relative to the particle kinematics are integrated in time using a standard fourth-order Runge-Kutta scheme, while the equations relative to the particle dymanics are solved using a mixed explicit/implicit differencing procedure developed by Ref. [42].

The Lagrangian particle tracking code exploits trilinear interpolation to obtain the fluid velocities at the particle position, using these velocities to advance the particle motion equations in time, with a time step size equal to that of the Eulerian fluid solver. For each tracked particle, the Euler parameters are renormalized at each time step as follows:

$$e_i = \frac{e_i}{\sqrt{e_0^2 + e_1^2 + e_2^2 + e_3^2}} \tag{15}$$

to preserve the constraint $e_0^2 + e_1^2 + e_2^2 + e_3^2 = 1$.

A. Flow domain

The flow domain is a channel in which the fluid is confined by two fixed top and bottom walls. In this study, four different geometric configurations are analysed. The first (reference) configuration is the one with smooth walls, while the other three configurations refer to rough walls with different mean amplitude of the roughness. Table I shows the geometric features of the computational domain for all configurations: the length along the streamwise (x_1), spanwise (x_2), and wall-normal (x_3) directions, the number of grid points used for discretization of the domain and the mesh resolution. As reported in Table I, for the smooth-wall channel (Case F1), the size of the computational domain is set to $2\pi\delta \times \pi\delta \times 2\delta$ in the streamwise, spanwise, and wall-normal directions, respectively. The domain length in the streamwise direction was duplicated for the rough-wall configurations (labeled as R1, R2, and R3, respectively, and corresponding to an increasing mean amplitude of the roughness). Periodic boundary conditions are imposed in the streamwise and spanwise directions, while the no-slip condition is enforced at the walls. The spatial distribution of the grid cells is uniform in the streamwise and spanwise directions, with grid cell size equal to $\Delta x_1^+ \approx 8.8$ and $\Delta x_2^+ \approx 4.4$, respectively. A nonuniform grid refinement strategy is used in the wall-normal direction, with minimum grid spacing of about 0.05 wall units at the wall and maximum grid spacing, at the channel centerline, of about 7 wall units at the channel centerline. Such grid spacing was chosen upon performing a grid sensitivity analysis, and was enforced both in the flat-wall case and in the different rough-wall cases, also considering that in rough conditions the mesh is boundary fitted. The reader is also referred to Ref. [83] for further details about the

TABLE II. Geometric parameters of the rough walls: $\bar{k}/\delta$ and $\bar{k}^+$ are the averaged absolute deviation of the heights of the rough walls, k_s/δ and k_s^+ are the equivalent sand-grain roughness, $k_{\max}/\delta$ and $k_{\max}^+$ are the highest roughness peaks and ES is the effective slope of roughness.

Case	Wall	$\bar{k}/\delta$	$\bar{k}^+$	k_s/δ	k_s^+	$k_{\max}/\delta$	$k_{\max}^+$	ES
F1	Smooth	–	–	–	–	–	–	–
R1	Rough (2D)	0.012	2.16	0.23	41.4	0.027	4.8	0.04
R2	Rough (2D)	0.024	4.32	0.29	52.2	0.065	11.7	0.09
R3	Rough (2D)	0.050	9.00	0.49	88.2	0.135	24.3	0.20

computational grid validation.We remark here that, in the present simulations, the Kolmogorov length scale has an average value of 2 wall units, its local value ranging from about 1.5 wall units near the wall to about 4 wall units at the channel centerline. Hence, the minimum grid spacing along the wall-normal direction, $\Delta x_{3,\min}^+$, is much smaller than the local Kolmogorov length scale.

The geometrical parameters of the rough walls are reported in Table II. Following Ref. [71], the height k of the 2D roughness, which represents the vertical distance from the horizontal reference surface located at $x_3 = 0$ and is a function of the streamwise direction x_1, is generated by superimposing n sinusoidal functions:

$$k(x_1) = \sum_{i=1}^{n} A_i \sin\left[\frac{2\pi x_1}{(L/2i)}\right], \tag{16}$$

where A_i and $L/2i$ are the amplitude and wavelength of the ith function, respectively. As in Ref. [83], a value $n = 4$ was used in the present study and cases R1 to R3 correspond to values of the normalized averaged absolute deviation:

$$\frac{\bar{k}}{\delta} = \frac{1}{L}\int_L |k(x_1)| dx_1, \tag{17}$$

equal to 0.012, 0.024, and 0.05, as also reported in Table II. To obtain the two-dimensional roughness, the geometry corresponding to $k(x_1)$ is extruded in the spanwise direction. We remark here that, in each rough channel case, the two walls have different local geometry but same roughness properties. Details on the roughness generation can be found in Ref. [100].

A 3D representation of the flow domains is provided in Fig. 2. The origin of the coordinate system is located at the bottom of the smooth channel, which also matches the location where the height variation associated with the wall undulations in the rough channels is equal to zero: positive height variations of the roughness correspond to peaks (colored in red), negative height variations of the roughness correspond to cavities (colored in blue).

B. Particle parameters

The geometric and physical properties of the dispersed particles are provided in Table III. The different particle sets have Stokes numbers ranging from $\mathrm{St}^+ = 1$ to 100, and aspect ratios ranging from $\lambda = 1$ (corresponding to the reference case of spherical particles) to 10. The semiminor axis of the particles was kept fixed among the sets and equal to $a^+ = 0.36$ in wall units, yielding a total of 12 cases examined. We remark here that the particles with aspect ratio $\lambda = 10$ have a dimensionless length $l^+ = 7.2$ in wall units, which corresponds to about 3.5 Kolmogorov length scales (considering the value of this scale as obtained upon volume-averaging over the entire flow domain). This is expected to introduce some degree of inaccuracy in the computation of the translational and rotational dynamics of these fibers, since the formulations we used to compute the forces and torques acting on each fiber are valid in the limit of linear velocity variations along the fiber length (this limit being verified when $l^+/\eta_K^+ \leqslant 1$, a condition that is met by the

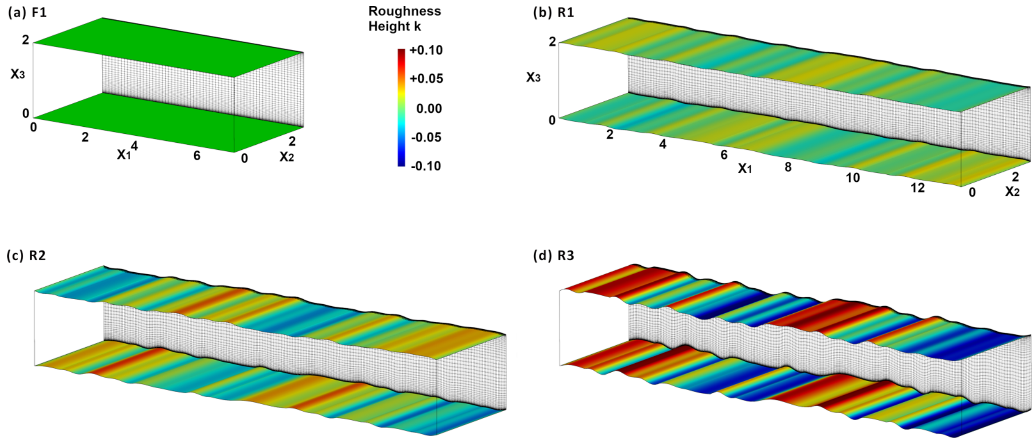

FIG. 2. 3D rendering of the four computational domains considered in this study. Walls are colored according to the amplitude of the roughness undulations. Peaks, characterized by $x_3 > 0$, are colored in red whereas cavities, characterized by $x_3 < 0$, are colored in blue. Areas where $x_3 = 0$ are colored in green. Panels: (a) Case F1, (b) Case R1, (c) Case R2, and (d) Case R3.

$\lambda = 1$ and $\lambda = 3$ fibers). The main effect will be on the computation of the torques, for which the formulation derived from Jeffery theory has been used. As shown by Ref. [46], the error incurred in the calculation of the torques can be computed as

$$\left|\left|\mathbf{M}_J^a - \mathbf{M}_J^c\right|\right| \approx 0.041\mathrm{St}^{+^{-0.34}}\left(\frac{l^+}{\eta_K^+}\right)^{1.44} \quad \text{for} \quad \frac{l^+}{\eta_K^+} < 8, \tag{18}$$

where $||\mathbf{M}_J^a - \mathbf{M}_J^c||$ is the global root-mean-square error incurred in the calculation of the Jeffery torques and η_K^+ is the volume-averaged Kolmogorov length ($\eta_K^+ \simeq 2$ in the present simulations). This formula yields an error of about 1% for all particles sets with $\lambda = 1$ and $\lambda = 3$. For $\lambda = 10$, the error ranges from about 5% when $\mathrm{St}^+ = 100$ to about 20% when $\mathrm{St}^+ = 1$. Clearly, for this latter particle set, our calculations cannot provide accurate statistics from a quantitative point of view and can only serve the purpose of showing trends.

TABLE III. Particle parameters: St^+ is the Stokes number, λ is the aspect ratio, S is the density ratio, $2b^+$ is the ellipsoid major axis, and ρ_p is the ellipsoid density.

Set	St^+	λ	S	$2b^+$	$\rho_p[\mathrm{kg/m^3}]$
P1-1	1	1	34.70	0.72	45.11
P1-3	1	3	18.57	2.16	24.14
P1-10	1	10	11.54	7.20	15.00
P5-1	5	1	173.60	0.72	225.68
P5-3	5	3	92.90	2.16	120.77
P5-10	5	10	57.70	7.20	75.01
P50-1	50	1	1736.0	0.72	2256.8
P50-3	50	3	929.0	2.16	1207.7
P50-10	50	10	577.0	7.20	750.1
P100-1	100	1	3469.91	0.72	4510.88
P100-3	100	3	1857.13	2.16	2414.26
P100-10	100	10	1154.21	7.20	1500.48

To ensure converged statistics, we tracked 200,000 particles per set, under the assumption of dilute flow conditions and, hence, one-way coupling between the phases. In all simulations, particles were initially distributed in the outer region of the computational domain, away from the rough walls to avoid initial trapping in the wall cavities, with random orientation and velocity equal to that of the fluid at the particle position. The nondimensional time window used to compute the particle statistics was equal to $\Delta t^+ = 10^5$ in wall units. Several tests were performed to check that the imposed initial conditions do not affect statistical convergence and to select the value of Δt^+.

As particles are brought about by turbulence, they obey periodicity conditions in the streamwise and spanwise directions and their collisions with the solid walls are modeled as purely elastic rebounds. In the smooth channel case, a rebound occurs whenever the distance between the center of mass of the particle and the wall is less than the vertical projection of the ellipsoid major axis. In the presence of rough walls, wall collisions are more complex to handle and require careful treatment. In this study, we use the collision algorithm developed by Ref. [101] to detect and implement collisions taking into account the local slope of the rough walls. The reader is also referred to Ref. [83] for additional details on the algorithm performance when applied to ellipsoidal particles.

III. RESULTS

In this section the combined effect of particle inertia, particle elongation and large-scale roughness is discussed from a statistical point of view, specifically examining particle velocity statistics, particle spatial distribution within the domain, particle preferential concentration, and particle preferential orientation with the flow. As known from the literature, particles with different inertia are transported differently by the fluid in bounded domains: low-inertia particles follow the fluid in a way similar to tracers and tend to remain uniformly distributed; high-inertia particles tend to drift toward the walls and undergo long-term accumulation there. Wall accumulation has been widely studied for the case of spherical particles [19,24,102] but has been observed also for ellipsoidal particles, which in addition exhibit preferential orientation in the inner region [15,23,50]. We expect this phenomenology to be altered by roughness, which is known from literature to significantly modify the spatial distribution as well as the velocity and orientation statistics of the particles. In the following, we discuss these modifications and quantify their magnitude as particle inertia is varied by two orders of magnitude and particle elongation is increased by one order of magnitude.

A. Velocity statistics

In this section, we analyze the particle velocity statistics, also in comparison with the Eulerian fluid velocity, to correlate the macroscopic particle distribution previously described with the mean features of the two-phase flow.

The mean streamwise velocity of the fibers is shown in Fig. 3 as a function of the vertical coordinate. Symbols refer to the different Stokes numbers, whereas the solid line refers to the Eulerian fluid velocity. Results show that the effect of elongation on this statistics is negligible, as in Ref. [83], and therefore we only show the results relative to the spherical particles. Note that negligible aspect ratio effects on the mean velocity were also reported in the experiments by Ref. [103] where, contrary to our case, the tracked particles were large enough to generate appreciable wake effects.

Each panel in Fig. 3 refers to one of the flow geometries considered in this study. In the smooth flat channel (case F1, panel a), the velocity profiles for the two lower Stokes numbers overlap almost perfectly with the fluid velocity profile, whereas inertia produces a slight velocity overshoot in the buffer layer for the two larger Stokes numbers. As soon as particles experience the effect of wall roughness (case R1, panel b), a sort of bimodal behavior can be observed: While the profiles of the two lower-inertia particle sets still follow the fluid velocity very neatly, the two sets with higher inertia are characterized by a large overshoot (which is also Stokes number dependent), probably due to the interaction with boundary peaks which prevent particles to interact with low-speed streaks.

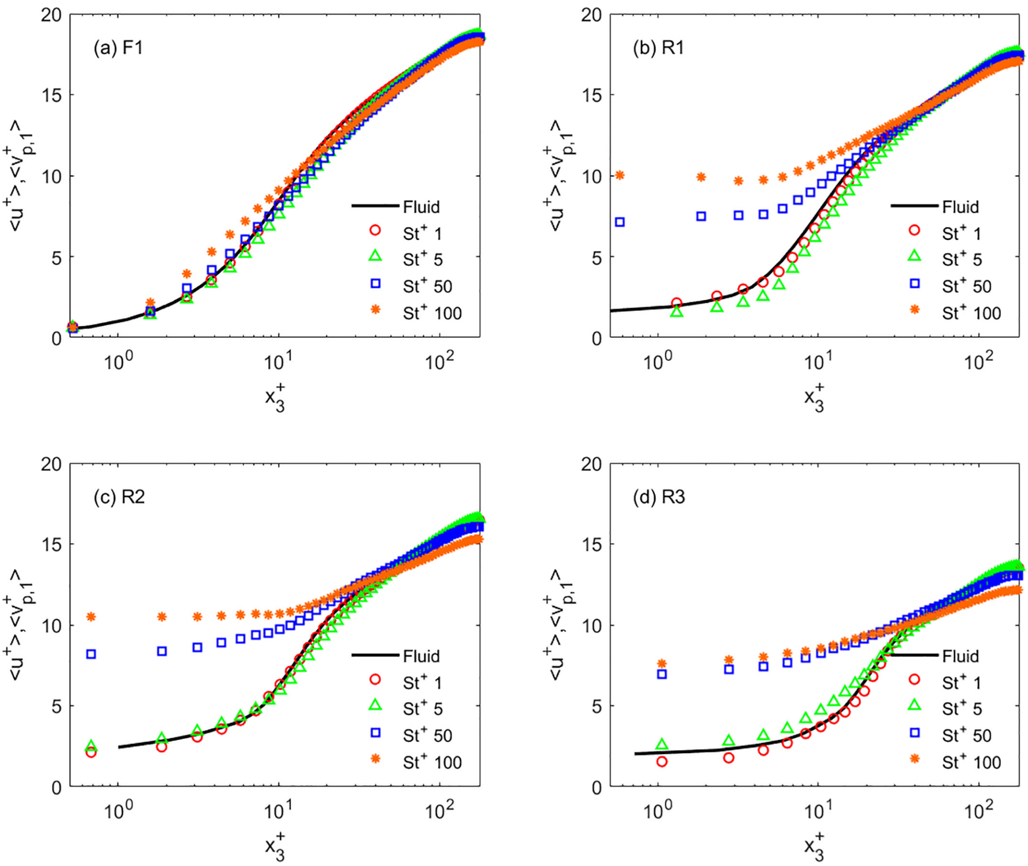

FIG. 3. Mean streamwise velocity of the particles with aspect ratio $\lambda = 1$. Panels: (a) Case F1, (b) Case R1, (c) Case R2, and (d) Case R3.

The situation is very similar in the case of intermediate wall roughness (case R2, panel c) with the exception of the $\mathrm{St}^+ = 100$ particles, which clearly lag the fluid outside of the buffer layer. The near-wall velocity overshoot is found to be milder and to lose its Stokes number dependence in the highest wall roughness case (case R3, panel d). Again, in the bulk of the flow, the particles with the largest inertia tend to move significantly slower than the fluid in the streamwise direction. These effects are a direct consequence of the roughness, which acts to modify the turbulent flow field by reducing velocity while increasing vorticity [66].

To investigate further the streamwise velocity difference between the two phases, in Fig. 4 we show the profiles of the slip streamwise velocity measured along the wall-normal direction. The slip velocity is defined as $\langle \Delta u^+ \rangle = \langle u_{1@p} \rangle - \langle v_{p,1} \rangle$, where angle brackets represent time and space average in the streamwise and spanwise directions. Figures 4(a) and 4(c) refer to spheres and elongated particles with $\lambda = 10$ in the smooth channel case, respectively; Figs. 4(b) and 4(d) refer to the very same particles sets in the rough channel case R3, respectively. In each panel, profiles refer to different values of particle inertia. As previously anticipated, comparison of Figs. 4(a) and 4(c) as well as Figs. 4(b) and 4(d) confirms that the effect of elongation on the mean velocity is not relevant: Changes in the slip velocity are ascribed to inertia and wall roughness only. This finding is in line with those of Ref. [104] for neutrally buoyant low-aspect-ratio particles in homogeneous isotropic turbulence and by Ref. [51] for heavy fibers in turbulent channel flow. In both cases, only minor quantitative effects of elongation on the wall-normal behavior of the slip velocity statistical moments

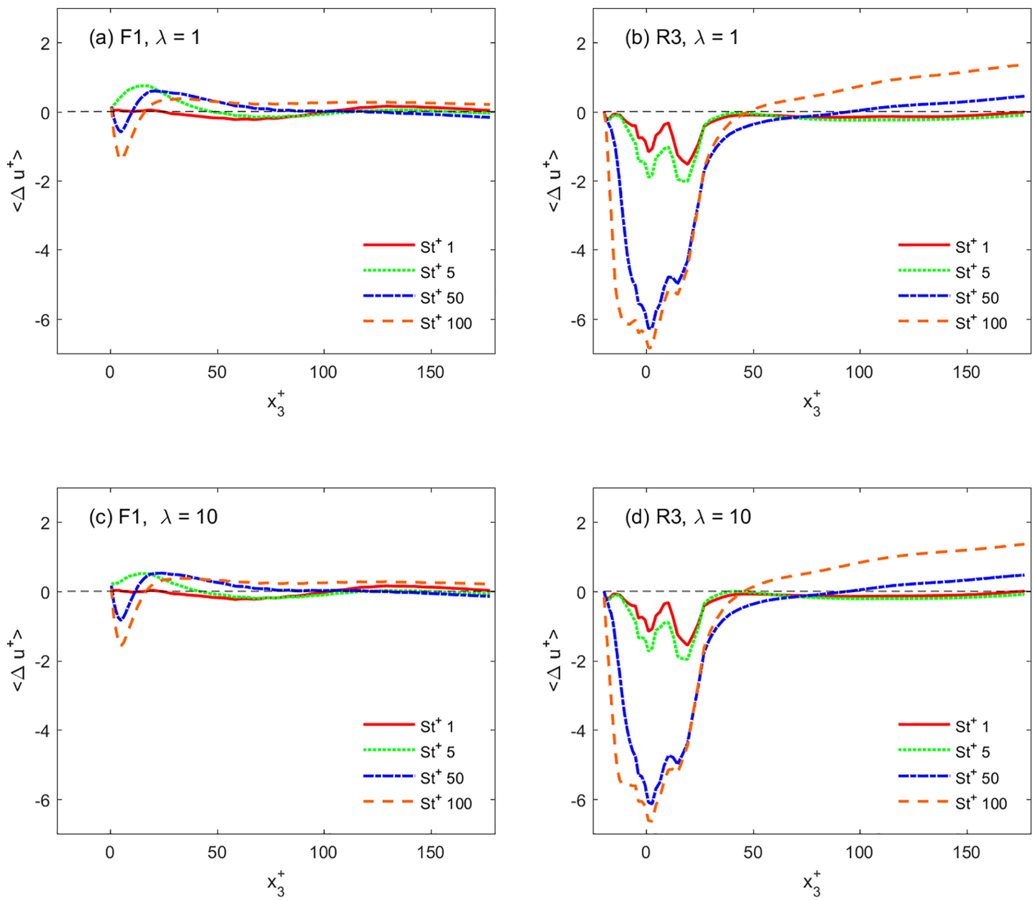

FIG. 4. Slip streamwise velocity at varying particle inertia along the wall-normal direction. Panels: (a) case F1 with $\lambda = 1$, (b) case R3 with $\lambda = 1$, (c) case F1 with $\lambda = 10$, and (d) case R3 with $\lambda = 10$.

were reported. In the present one-way coupled simulations, the reason for this counterintuitive result is related to the fact that the spatial distribution of the particles is controlled by their tendency to concentrate in specific regions of the flow, namely in regions of low vorticity and high strain rate when the centrifuge effect of vortices prevails or in regions of zero fluid acceleration when the sweep-stick mechanism prevails [13]. On average, turbulence acts to always cluster particles in these regions and, therefore, both the mean fluid velocity sampled at the particle position and the mean particle velocity do not change significantly for a given value of particle inertia. It should be recalled that the mean velocities are obtained upon volume-averaging along the streamwise and spanwise directions and upon time-averaging. In addition, averaging is performed considering a lumped-parameter model in which the particle velocity is available at the particle center of mass, regardless of its aspect ratio. These operations definitely contribute to the filtering of the fluid and particle velocity fluctuations, which may be more substantially affected by particle length.

Focusing now on inertia, we observe that the main effects are produced inside the buffer layer when the channel walls are smooth: Examining Figs. 4(a) and 4(c) it is clear that the slip velocity for the $\mathrm{St}^+ = 1$ particles is everywhere very close to zero and deviations from zero slip can be safely considered to be negligible. The slip velocity for the $\mathrm{St}^+ = 5$ particles is positive in the buffer layer but then vanishes in the bulk of the flow ($x_3^+ > 50$). The only particles for which a significant negative slide velocity near the wall and positive slip velocity in the buffer layer ($10 < x_+^3 < 50$) are those with $\mathrm{St}^+ = 50$ and 100. Note that the sign changes occur at locations that vary with particle inertia. Local positive/negative peak values of $\langle \Delta u^+ \rangle$ are also Stokes number dependent. Particles with higher inertia lead the fluid neat the wall, indicating preferential accumulation in high-speed regions and possibly short residence times (long-term trapping in the near-wall region is associated with particle accumulation in low-speed regions), and lag the fluid in the buffer layer, indicating preferential accumulation in fluid ejections. Inertial effects for the $\mathrm{St}^+ = 50$ and 100 particles are magnified and extend to the entire channel section in case the walls are rough, as can be seen examining Figs. 4(b) and 4(d). First off, the magnitude of the slip velocity becomes significantly larger (now showing a significant gap between the two lower-inertia sets and the two higher-inertia sets) and the region with negative slip velocity values widens, exhibiting a peak at $x_3^+ = 0$. In addition, a significant increase of $\langle \Delta u^+ \rangle$ beyond $x_3^+ = 50$ is observed at increasing Stokes number. Overall, these observations confirm the decorrelation between the motion of the particles and the motion of the surrounding fluid that inertia and roughness produce.

To correlate the streamwise particle motion with the wall-normal particle motion, in Fig. 5 we show the probability density function (PDF) of the wall-normal particle velocity, v_{p_3}. The PDF refers to the steady state of particle–wall-normal distribution and is conditioned to particles located in the buffer layer ($5 < x_3^+ < 30$), where the most interesting effects associated to inertia and roughness occur. The PDFs are shown for all the flow configurations and all the particle Stokes numbers considered in this study, whereas only two values of the aspect ratio are reported: $\lambda = 1$ (left-end panels) and $\lambda = 10$ (right-end panels). We remind here that positive (respectively, negative) values of v_{p_3} indicate particles moving away from (respectively, to) the wall.

Considering the smooth-wall case first, shown in Figs. 5(a) and 5(b), we observe a rather narrow and symmetric PDF that peaks at $v_{p_3} = 0$ and is little affected by particle elongation. This latter result agrees well with the experimental findings of Ref. [15], where the distribution of the particle–wall-normal velocity in the buffer layer was found to be unaffected by differences in particle length and the reason was attributed to the strong alignment attained by the particles along the streamwise direction. Our findings, once combined with those of Ref. [103] on velocity fluctuations, suggest that aspect ratio effects on the fluctuating part of the velocity field may be directly correlated to the capability of elongated particles to produce localized wake dynamics within the flow. Interestingly, the PDF exhibits wider tails for the lower-inertia particles. These observations indicate that the majority of the particles moves within the buffer layer with little vertical velocity and that intense vertical motions are more likely if particles are able to follow the coherent sweep and ejection fluid events, responding to all fluid velocity fluctuations instead of filtering them out. As soon as particles start interacting with a rough wall, the PDF is modified, especially in its right tail. In the R3 case, with low wall roughness, the peak is still located at $v_{p_3} = 0$ but the monotonic dependence on the Stokes number is lost since the right tail of the PDF shifts toward larger values for the two higher-inertia sets, as shown in Figs. 5(c) and 5(d). For large enough inertia, particles may leave the buffer layer with much higher velocities. This is a result of their interaction with the roughness asperities, since the left tail of the PDF (associated to particles moving to the wall) appears to be very weakly affected by the change of wall geometry, as also discussed in Ref. [82]. As roughness increases, the PDF widens for all particle sets, but particularly for the higher-inertia particles, which exhibit a remarkable growth of the right tail (as can be appreciated from Figs. 5(e)–5(h)). Interestingly, the PDF of the $\mathrm{St}^+ = 100$ particles has also a wider left tail. This is clearly an effect of particle interaction with wall roughness, possibly hinting to the presence of particles in free-flight from one wall to the other. Note that the much wider range of both positive and negative wall-normal velocities sampled by the particles in the presence of roughness is in agreement with the reduction of the particle residence time in the viscous sublayer that roughness is known to induce [83]: Particles may travel vertically through the buffer layer with high velocities and, hence, reduce their residence time in their near-wall region.

A final comment on the weak dependence of the PDFs on λ is in order. The secondary role played by λ on the particle–wall-normal velocity distribution could be anticipated for large St^+, when inertial effects are dominant on particle transport, but is not straightforward to explain for

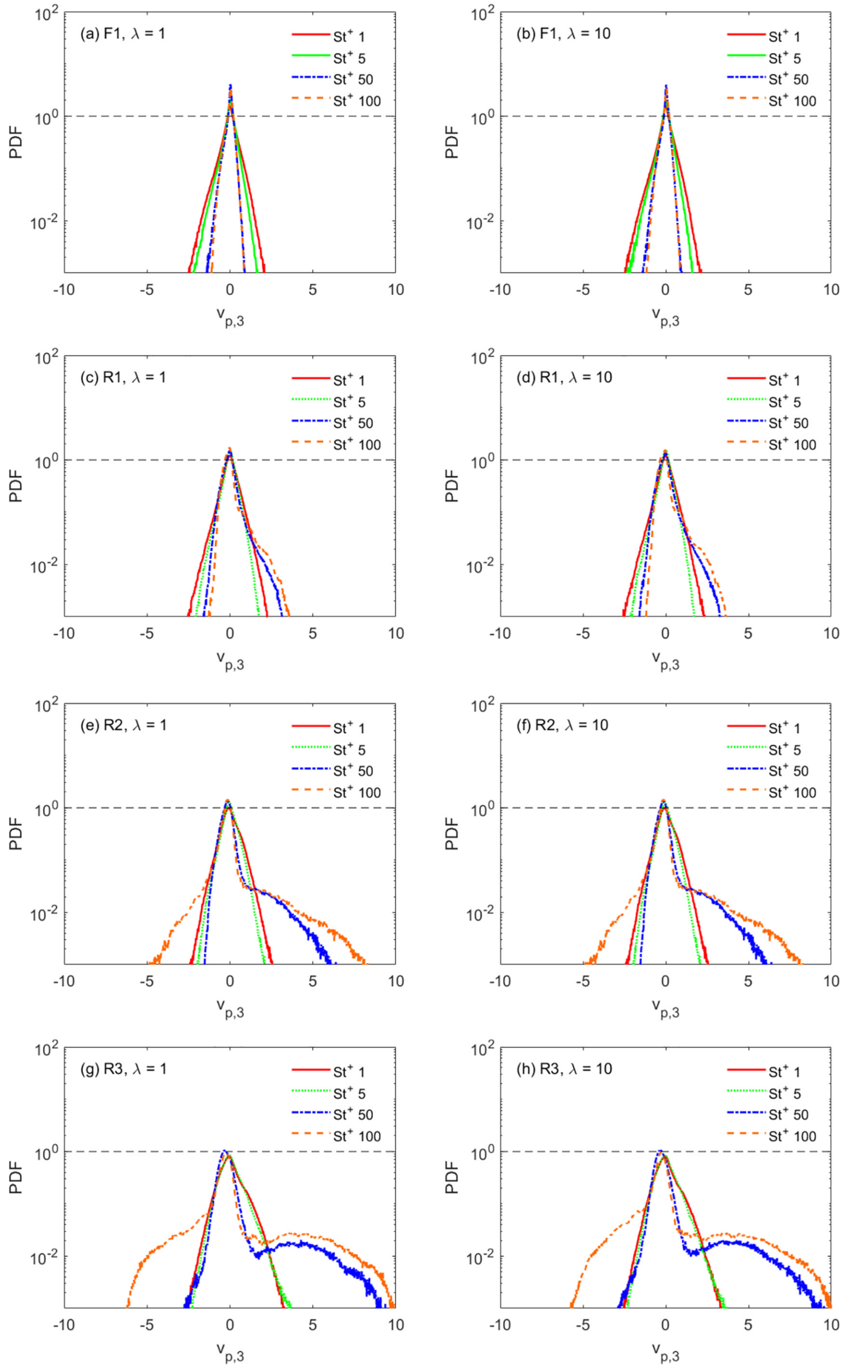

FIG. 5. PDF of the wall-normal particle velocity in the buffer layer ($5 < x_3^+ < 30$) at statistically steady state. All channel flow configurations and all Stokes numbers are shown. Panels: (a) case F1 with $\lambda = 1$; (b) case F1 with $\lambda = 10$; (c) case R1 with $\lambda = 1$; (d) case R1 with $\lambda = 10$; (e) case R2 with $\lambda = 1$; (f) case R2 with $\lambda = 10$; (g) case R3 with $\lambda = 1$; (h) case R3 with $\lambda = 10$.

the smaller St^+ considered in our simulations. If one looks at the effect of λ in isolation from other particle parameters, then it is easy to observe that an increase of aspect ratio leads to an increase of the drag force acting on the particle (due to an increase of the diagonal elements of the resistance tensor $\mathbf{K}$), but also corresponds to a larger particle mass (namely, to higher momentum for a given particle velocity). Fig. 5 hints to the possibility that these two effects balance each other, such that a particle with large mass can acquire higher momentum in the bulk of the flow but is then subject to a stronger resistance once in the buffer layer due to higher drag. In this case, particle acceleration would be unaffected (or just slightly affected) by a change in particle length at fixed particle inertia. This conclusion would be in qualitative agreement with the lack of shape effects on the mean translational acceleration of nearly neutrally buoyant spheres, fibers and disks observed in the experimental measurements of Ref. [105], but also with the numerical findings of Ref. [58], who computed acceleration statistics of prolate spheroidal particles in turbulent channel flow, with Stokes numbers and aspect ratios similar to those considered in our study albeit at much higher shear Reynolds number ($\mathrm{Re}_\tau = 1440$). In this latter work, in particular, the effect of particle elongation was not clearly discernible for all acceleration components, except on the tails of the acceleration PDFs. All of these observations suggest that, once filtering effects due to increasing particles response time are excluded, particle transport is also controlled by sampling effects due to the tendency of particles to reside longer in specific regions of the flow. Indeed, the weak dependence of the PDFs on λ that we observe in the buffer layer corroborates the conclusion that, once in the buffer layer, particles tends to occupy the same regions of the flow and are thus exposed to similar turbulent fluctuations.

B. Mean particle motion

In this section we examine the influence of elongation, inertia and roughness on the total particle mass flux, which we quantify here by means of the average bulk velocity of the particles along the streamwise direction. This velocity is computed as

$$v_b = \frac{1}{N_p} \sum_{k=1}^{N_p} v_{p_1,k}, \tag{19}$$

where $v_{p_1,k}$ is the streamwise velocity of the kth particle and N_p is the total number of particles tracked for each value of St^+ and λ. The values of v_b, normalized by the average bulk velocity of the fluid, u_b, are reported in Fig. 6 and compared with the values obtained by Refs. [75,82] for spherical particles. In particular, the study by Ref. [75] considers spherical particles with Stokes number ranging from 0.1 to 50 in turbulent channel flow at $\mathrm{Re}_\tau = 180$ bounded by walls with a two-dimensional roughness similar to that of our work (the average roughness height being $\bar{k}^+ = 9$, which is similar to the present case R3). The study by Ref. [82], however, considers spherical particles with Stokes number ranging from 1 to 1000 in a turbulent pipe ($\mathrm{Re}_\tau = 180$) bounded by a wall with three-dimensional regular roughness of average height $\bar{k}^+ = 2 \div 8$, a range that is very close to the one considered in our study. To make a meaningful comparison, we focus the discussion on the spherical particles. However, our results (not shown for sake of brevity) demonstrate that elongation does not affect the average bulk velocity of the particles and, hence, results for $\lambda = 1$ are very similar to those obtained for $\lambda = 3$ and $\lambda = 10$ (for the same reasons that explain the lack of length effects on the particle velocity statistics shown in Figs. 3–5). At low St^+, one finds $v_b/u_b \simeq 1$ for all the three flow configurations examined, which is expected when the inertial bias is small. As St^+ is increased, the effect of turbophoresis sets in and particle deposition is enhanced: This leads to a reduction of v_b, which attains a minimum for Stokes numbers roughly in the range $10 \leqslant \mathrm{St}^+ \leqslant 100$, followed by a final increase. The inclusion of roughness alters this behavior, leading to much smaller variations of v_b at varying particle inertia and producing a slight increase of v_b in the range $10 \leqslant \mathrm{St}^+ \leqslant 100$. From a quantitative point of view, our results match very well those of Ref. [82] at low roughness [$\bar{k}^+ = 2$, Fig. 6(b)] but exhibit some discrepancies at both intermediate [$\bar{k}^+ = 4$, Fig. 6(c)] and high roughness [$\bar{k}^+ = 9$, Fig. 6(d)] for the two lower-inertia

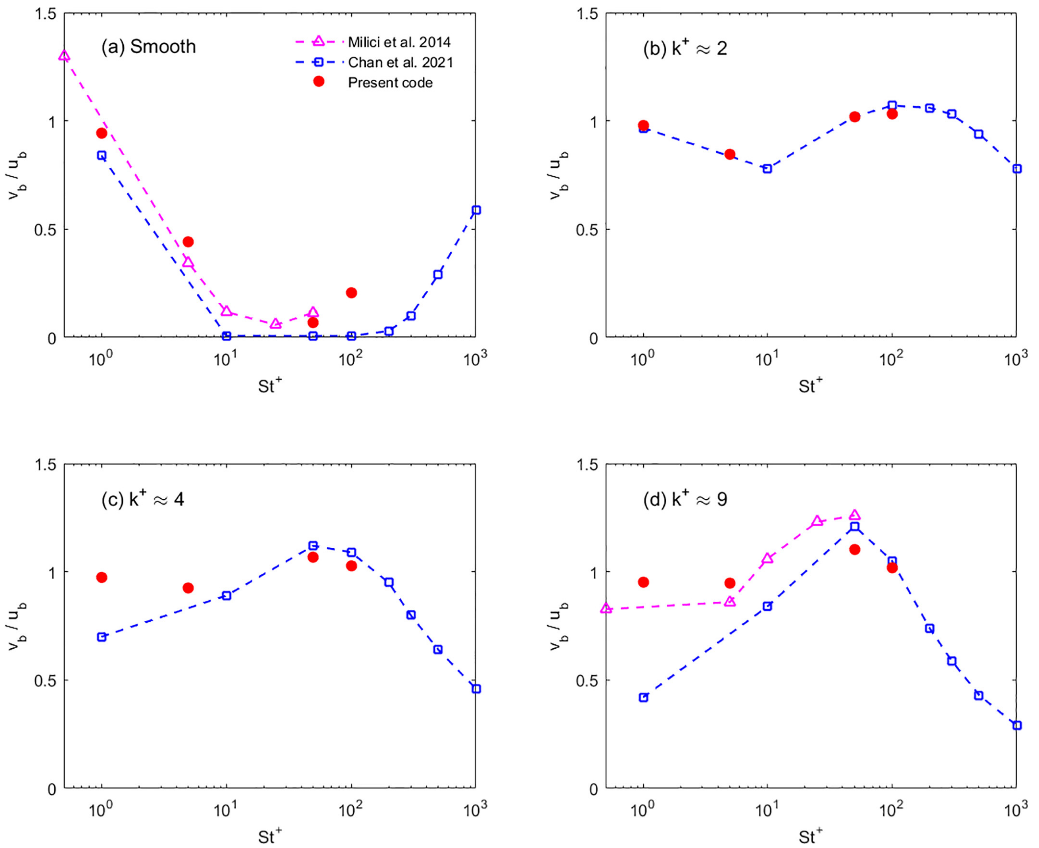

FIG. 6. Average streamwise bulk velocity of the particles ($\lambda = 1$), normalised by the fluid bulk velocity, as a function of the particle Stokes number St^+. Panels: (a) smooth walls; (b, c, d) rough walls with increasing average roughness height $\bar{k}^+$.

particle sets. More specifically, our simulations predict higher values of v_b (and closer to the bulk fluid velocity). This can be ascribed to the fact that, in our simulations, fewer particles get trapped in the cavities of the roughness and hence move with higher streamwise velocity. In turn, such a reduced trapping can be explained considering the different (three-dimensional) type of roughness considered by Ref. [82] and the resulting different geometry of the domain. This conclusion is supported by the good agreement of our results with those by Ref. [75], who also considered two-dimensional roughness [see Fig. 6(d)]. The change of v_b at varying St^+ in the rough-wall cases is a direct consequence of particle interaction with the walls, which favour resuspension and mixing of the dispersed phase in the central region of the channel. Note, however, that the results of the three studies under comparison agree well at high Stokes numbers, indicating that the type of roughness is not an important factor at large-enough particle inertia.

C. Particle spatial distribution

A visual rendering of the instantaneous particle distribution within the flow domain is provided in Fig. 7. In this figure, we wish to focus our attention on the qualitative effect of roughness and inertia. Therefore, only two particle sets (spherical particles with $\mathrm{St}^+ = 1$ and $\mathrm{St}^+ = 100$) and two flow configurations (case F1 with smooth walls and case R3 with highly rough walls) are presented. The figure panels provide a side view of particle distribution, showing a slice of the flow taken in the

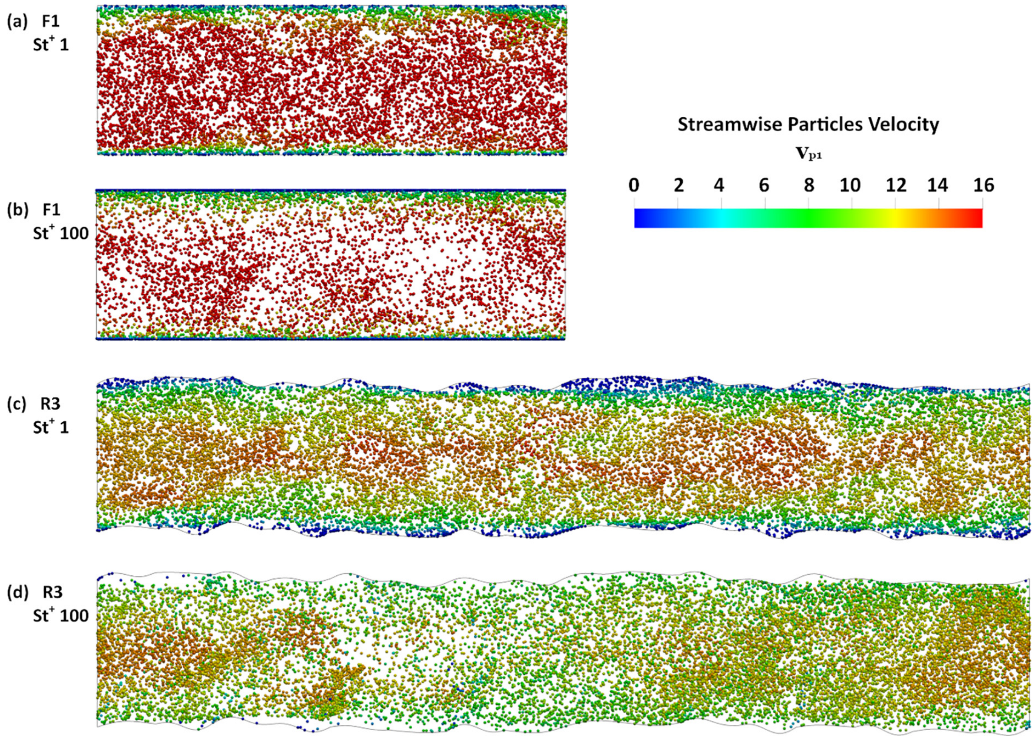

FIG. 7. Side view (x_1-x_3 plane) of the instantaneous particle distribution. Only particles located within a distance of 15 wall units from the $x_2 = 100$ plane are shown. Panels: (a) Case F1 and Set P1-1, (b) Case F1 and Set P100-1, (c) Case R3 and Set P1-1, (d) Case R3 and Set P100-1.

x_1-x_3 plane at $\Delta^+_{x_2} = 100 \pm 15$. Particles are colored according to their streamwise velocity, v_{p_1}. As expected, comparison of Figs. 7(a) and 7(b) clearly shows that particles with small Stokes number in the smooth-wall channel are randomly distributed throughout the domain, whereas particles with $\mathrm{St}^+ > 1$ undergo preferential concentration and accumulate at the wall [17,102,106]. This results in a much lower number of fast moving particles in the bulk of the flow.

Focusing our attention on the rough walls case, shown in Figs. 7(c) and 7(d), it is clear that the main macroscopic effect of roughness is to homogenize particle distribution, this effect being particularly evident in the case of the high-inertia (heavier) particles. As a result of this homogeneization, a strong reduction of particle velocity is observed in the bulk of the flow compared to the smooth flat channel case. Interestingly, we observe that the low-inertia particles are able to reach the cavities of the rough walls, where their streamwise velocity is very low (possibly indicating long-term trapping), whereas high-inertia particles accumulate much less in such pockets of the flow. Figure 7 highlights the different degree of nonuniformity attained by particle concentration in the different flow configurations. Roughness tends to redistribute particles throughout the domain, thus producing a smoothening of the concentration profiles. Without roughness, much higher peaks of concentration (namely, higher number density of particles per unit volume of fluid) can be observed near the wall. This is due to the different turbophoretic drift experienced by the particles: Those with higher inertia acquire higher wall-normal velocity fluctuations as their distance from the wall increases and this results in a stronger migration to the wall. As shown by Ref. [107], this effect may be partially counterbalanced by the biased sampling of near-wall regions, which acts to preferentially concentrate particles in areas of outward-moving fluid thus inducing migration of particles away from the wall. When particles accumulate in the cavities, however, they see

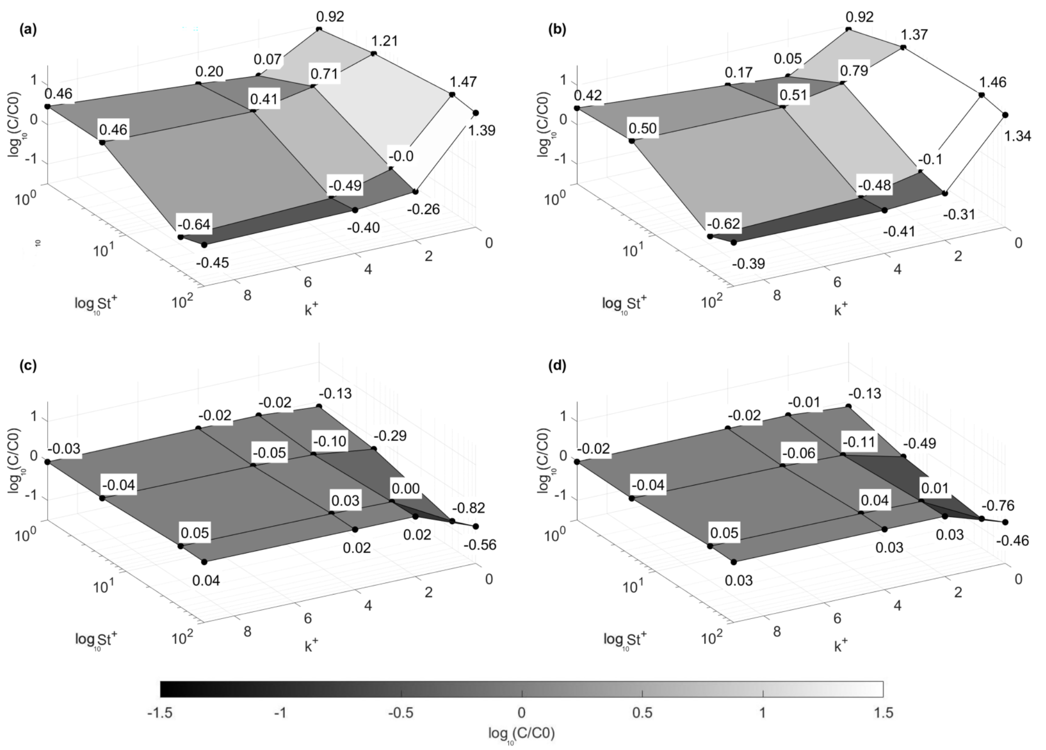

FIG. 8. Mean particle concentration in the viscous sublayer ($x_3^+ < 5$, top panels) and in the outer layer ($x_3^+ > 30$, bottom panels). Panels (a) and (c) refer to particles with aspect ratio $\lambda = 1$; panels (b) and (d) to particles with aspect ratio $\lambda = 10$.

much lower wall-normal fluid velocities and hence experience a reduced biased-sampling effect. In terms of velocity distribution, a marked difference is observed also in the bulk of the flow, where low-inertia particles appear to move faster than high-inertia ones.

D. Preferential concentration

In this section, we examine the influence of particle inertia, particle elongation and wall roughness on particle spatial distribution. We consider two specific regions of the flow: The viscous sublayer (namely, the fluid slab within the wall and the location $x_3^+ = 5$) and the outer layer (namely, the fluid slab beyond $x_3^+ = 30$). Within each region, the mean value of the particle concentration at steady state is computed upon volume-averaging over the particles instantaneously located in each region and time-averaging the resulting instantaneous values over a window of 1000 wall time units (this second averaging removes the concentration fluctuations around the steady-state value). By doing so, we obtain a mean value for each combination in the (St^+, λ, $\bar{k}^+$) parameter space. The outcome of this calculation is shown in Fig. 8, where each panel refers to a given value of λ (either $\lambda = 1$ or $\lambda = 10$). The logarithmic value of the mean concentration C, normalized by its initial value $C_0 = C(t = 0)$, is reported on the vertical axis. Note that $\log(C/C_0) > 0$ [respectively, $\log(C/C_0) < 0$] indicates accumulation (respectively, depletion) of particles within the monitor region over time. The different values of the Stokes number St^+ and of the averaged absolute deviation of the heights of the rough walls $\bar{k}^+$ are reported on the horizontal axes. The grayscale map provides a visual rendering of the expected change in concentration at varying St^+ and $\bar{k}^+$: dark gray areas correspond to small changes of C/C_0, whereas white and light gray areas correspond to large changes of C/C_0 for relatively small variations of St^+ and $\bar{k}^+$.

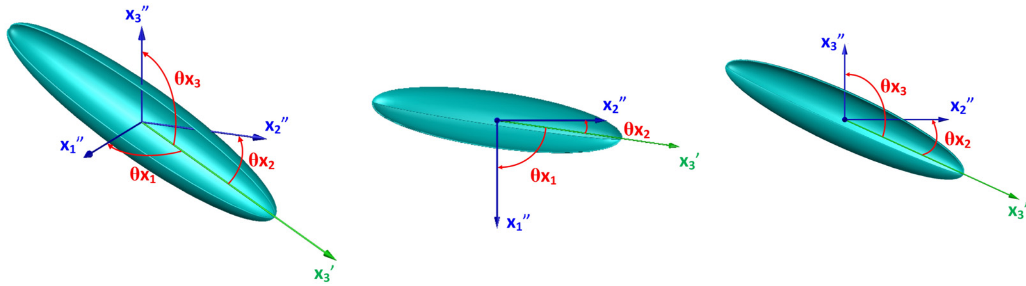

FIG. 9. Schematic representation of the angles Θ_{x_i} used to compute the direction cosines.

Focusing the attention on Fig. 8(a), which refers to the spherical particles inside the viscous sublayer, we observe that preferential concentration is maximum for a combination of small (or zero) values of $\bar{k}^+$ and large values of St^+ ($\mathrm{St}^+ > 10$ for the cases simulated in the present study). This maximum is produced by turbophoresis, which is very efficient in trapping particles in the viscous sublayer. We also observe that, regardless of the Stokes number, high peaks of concentration are prevented by large-enough roughness ($\bar{k}^+ > 3$ for the cases simulated in the present study). This happens because wall roughness is now able to provide an additional resuspension mechanism by transferring enough momentum from the horizontal direction into the vertical direction. Particle depletion in the viscous sublayer is observed to occur when both $\bar{k}^+$ and St^+ are large, as a result of the enhanced mixing that occurs when highly inertial particles interact with highly rough walls. Interestingly, there is a combination of values for $\bar{k}^+$ and St^+ that keeps the particles randomly distributed, this condition being associated to vanishing values of $\log(C/C_0) < 0$. Similar observations can be made for the elongated particles with $\lambda = 10$. As can be seen upon comparison of Fig. 8(b) with Fig. 8(a), an increase of aspect ratio produces only quantitative changes in the particle concentration, the most notable being the extension of the maximum preferential concentration to values of St^+ below 10. A completely different scenario is offered by Figs. 8(c) and 8(d), which refer to the outer layer. In this case, the presence of rough walls prevents a strong depletion of particles and leaves the particle number density substantially unchanged as compared to the smooth-wall case. This is clearly associated to a roughness-driven homogenization of particle distribution throughout the channel height. Only for small or vanishing roughness, inertia plays a role in keeping the particle concentration constant or nearly constant. As could be expected, particle length plays a very minor role on the preferential concentration of particles residing in the outer layer. This finding is consistent with recent experiments [15,16,103].

E. Particle orientation and alignment with the flow

The statistical observables examined in the previous sections did not exhibit any significant dependence on particle elongation. In this section, we examine the particle orientation statistics, for which elongation is expected to play a role. Specifically, we look at the mean direction cosines, which provide a measure of particle preferential alignment with the flow, and the orientation frequencies, which provide a measure of the likelihood associated to a certain orientation state, and hence on possible preferential alignment with the mean flow direction [50].

The direction cosines are obtained from the angles Θx_i that the major axis of the particle (namely, the axis x_3' of the Lagrangian frame of reference) forms with the axes x_i'' of the comoving frame, as shown in Fig. 9. A particle is thus aligned with the ith flow direction when $\cos|\Theta x_i| = 1$ (for ease of notation, the absolute value symbol will be dropped hereinafter).

When confined within smooth walls, ellipsoidal particles are known to orient themselves along the mean flow direction in the near-wall region and to sample uniformly the three-dimensional orientation space in the central region, driven by the randomizing action of the turbulence [50].

Both inertia and elongation contribute to modify the strength of the near-wall alignment, which can typically be maintained only for finite times, but become much less important for particle orientation in and beyond the logarithmic layer [50].

The effect of roughness, albeit in isolation from inertia (the only Stokes number considered was $\mathrm{St}^+ = 5$), has been evaluated by Ref. [83], who showed that highly rough walls tend to align particles with their major axis close to the x_1-x_2 plane, inducing a more uniform orientations than in the presence of smooth walls. This isotropization of particle orientation was found to be limited to the near-wall region.

Here, we extend the analysis of Ref. [83] by including all three factors: inertia, elongation and roughness. Since these factors play a role only close to the wall, the orientation statistics discussed in this section were computed considering only particles instantaneously located within a distance $x_3^+ < 30$ from the walls.

The mean direction cosines obtained upon volume-averaging over such reference volume (and upon time-averaging as well) are shown in Fig. 10, as a function of inertia (St^+, horizontal axis) and roughness ($\bar{k}^+$, vertical axis). Each panel refers to a fixed value of the aspect ratio: $\lambda = 3$ for the left-end panels (a), (c), and (e); $\lambda = 10$ for the right-end panels (b), (d), and (f). Results for spherical particles are not shown because the value of the mean direction cosines is $\cos\Theta x_i \approx 0.5$ for all the simulated cases, which is the value of a full 3D isotropic distribution of orientations.

Considering the streamwise direction cosine first, it is apparent that ellipsoidal particles with small aspect ratio [Fig. 10(a)] exhibit a rather weak tendency to align with the mean flow direction of motion, regardless of inertia and roughness: The value of $\cos\Theta x_1$ is always comprised between 0.6 and 0.7, and no sharp peak is observed. Longer particles, however, may undergo stronger alignment for a combination of intermediate inertia, $\mathrm{St}^+ \sim \mathcal{O}(10)$, and intermediate roughness, $\bar{k}^+ \simeq 2$ [see Fig. 10(b)]. At small St^+, roughness modifies quantitatively the alignment but no effect can be observed at $\mathrm{St}^+ \sim \mathcal{O}(10^2)$.

In the spanwise direction, all three factors appear to matter. For the $\lambda = 3$ particles [Fig. 10(c)], some alignment is produced by roughness at small Stokes numbers.

Yet, the main effect is the disalignment produced by inertia at small or intermediate roughness. For the $\lambda = 10$ particles [Fig. 10(d)], the alignment becomes stronger over a wider portion of the plot, being favored by an increase of inertia at high roughness, whereas the disalignment at high Stokes numbers becomes much weaker and limited to the highest-inertia particles considered in this study.

Finally, in the wall-normal direction, we observe a rather strong tendency of the $\lambda = 3$ particles [Fig. 10(e)] to align with this direction at large Stokes numbers, the effect of roughness being secondary. At low Stokes numbers, roughness prevails and randomizes particles orientation. Again, a change in particle elongation produces a remarkable modification of particle orientation with the wall-normal direction, which becomes much less pronounced at large Stokes and is completely lost at low Stokes. Overall, Fig. 10 shows that the mean orientation of the ellipsoidal particles differs substantially from that of the spherical particles, and that inertia, elongation and roughness all contribute significantly to the different orientation states attained by the particles. Interestingly, the results of Fig. 10 suggest that long particles with high inertia exhibit weak tendency to align with the mean flow and stronger tendency to align with the vertical direction when interacting with low-roughness walls. However, when their inertia is decreased, preferential alignment is attained with the spanwise direction, possibly hinting to a change in the mode of rotation: from pole-vaulting to log-rolling [35].

As already shown by Ref. [50], the analysis of the mean direction cosines alone does not provide a direct indication of the probability with which preferential alignment along a flow direction can be attained over the observation time window. In other words, it cannot measure how often a certain preferential alignment is attained by the particle. In the case of rigid fibers in turbulent channel flow within smooth walls, for instance, the preferred condition of streamwise alignment with the near-wall mean flow is unstable and can be maintained for rather short times before fibers are forced to rotate around the spanwise axis by the shear-induced wall-normal velocity gradient

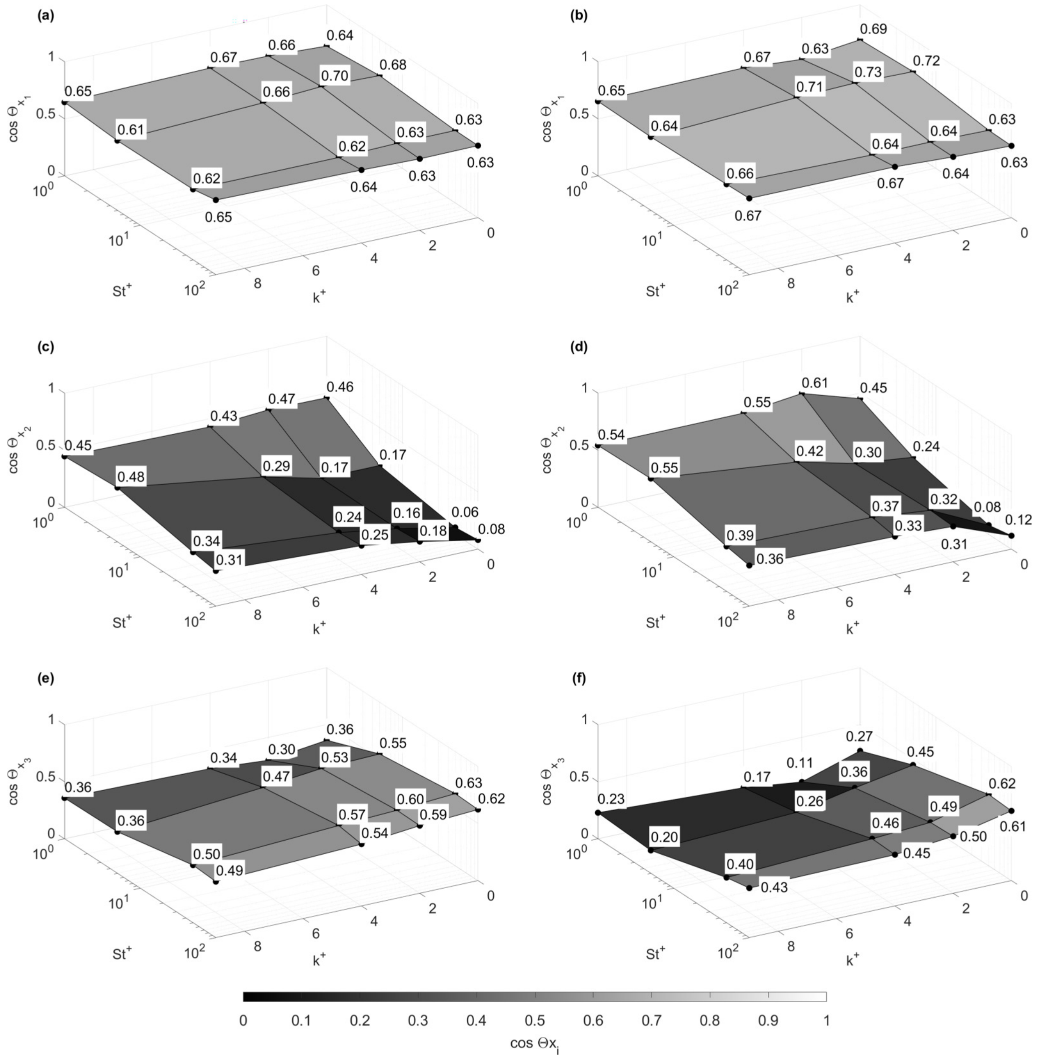

FIG. 10. Absolute value of the mean direction cosines in the near-wall region ($x_3^+ < 30$). Top-row panels refer to the streamwise direction cosine, $\cos \Theta x_1$; middle-row panels to the spanwise direction cosine, $\cos \Theta x_2$; and bottom-row panels to the wall-normal direction cosine, $\cos \Theta x_3$. Left-end panels refer to particles with aspect ratio $\lambda = 3$, right-end panels to particles with aspect ratio $\lambda = 10$.

[50]. With rough walls, this preferential alignment seems to become even more unstable, as shown by Ref. [83] albeit only for one value of particle inertia. Here, we examine the time persistency of preferential alignment by looking at the *orientation frequency*, defined as the percentage of time spent by a particle in a given position of alignment with one flow direction. In particular, in Figs. 11 and 12 we show the orientation frequency associated to the streamwise and spanwise direction cosines, respectively. We remark here that the directions cosines discussed in Fig. 10 are all ensemble-averaged over a subset of particles (those instantaneously located within 30 wall units from the walls) and then time-averaged. The orientation frequency, however, is computed without ensemble-averaging and without time averaging: It tells us the likelihood of a given alignment or—more generally—orientation state, the average of which corresponds to the value shown in Fig. 10. From Fig. 10 alone, one cannot infer anything about the likelihood of observing a certain

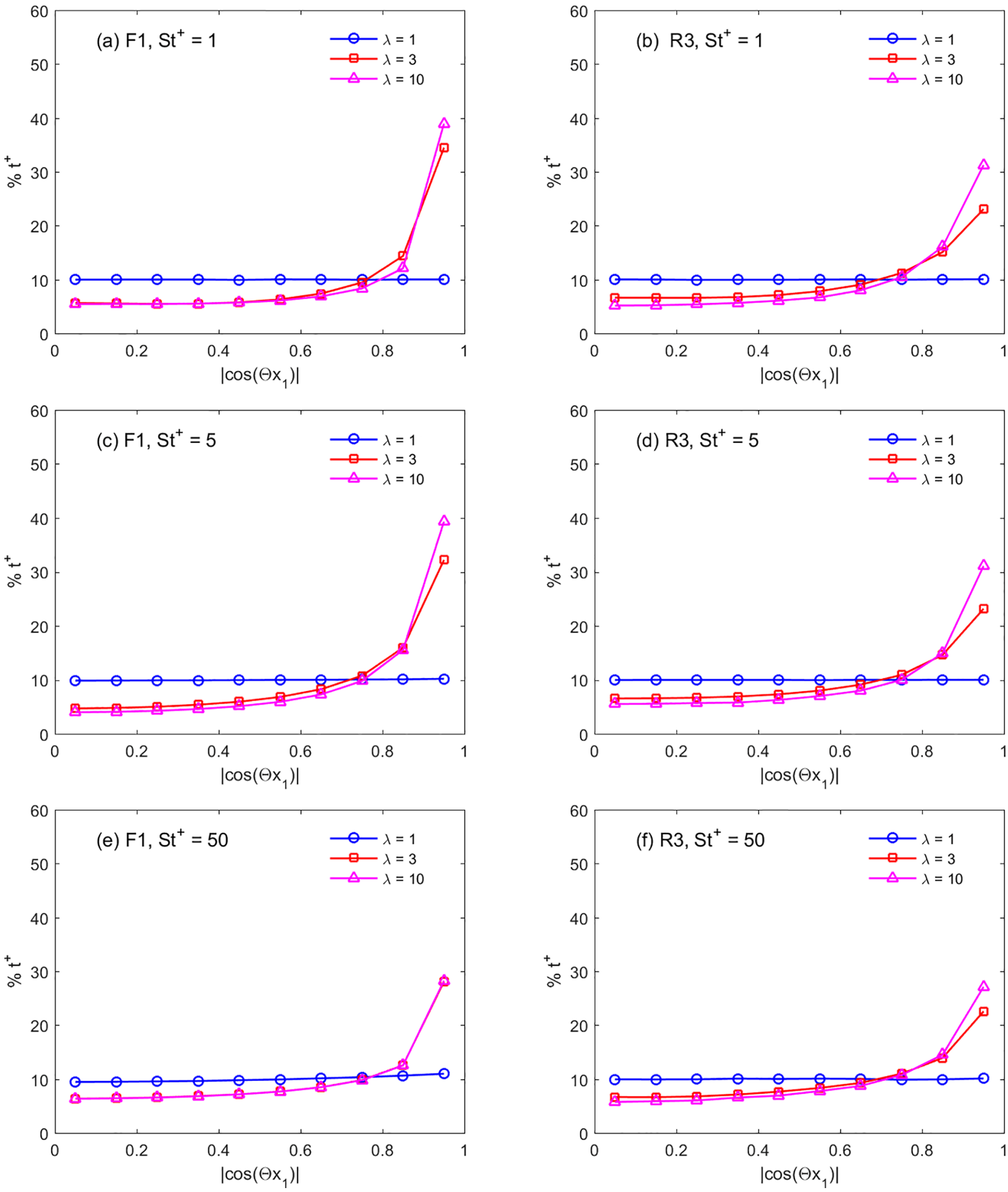

FIG. 11. Streamwise orientation frequency (percent values) in the near-wall region ($x_3^+ < 10$). Panels: (a) Case F1—St$^+ = 1$, (b) Case R3—St$^+ = 1$, (c) Case F1—St$^+ = 5$, (d) Case R3—St$^+ = 5$, (e) Case F1—St$^+ = 50$, (f) Case R3—St$^+ = 50$.

alignment/orientation within the flow. Results in Figs. 11 and 12 are relative to the region closest to the walls ($x_3^+ < 10$) and allow direct comparison between the smooth-walls case F1 (left-end panels in Figs. 11 and 12) and the rough-walls case R3 (right-end panels in Figs. 11 and 12) for St$^+ = 1, 5$, and 50 and for all values of λ considered in this study (note that results for St$^+ = 100$ are not shown because they are very close to those for St$^+ = 50$). By doing so, we extend the analysis done in Ref. [83] by spanning two orders of magnitude for St$^+$ to evaluate the interplay among roughness, elongation and inertia. The orientation frequency calculation procedure is the same of Refs. [50,83],

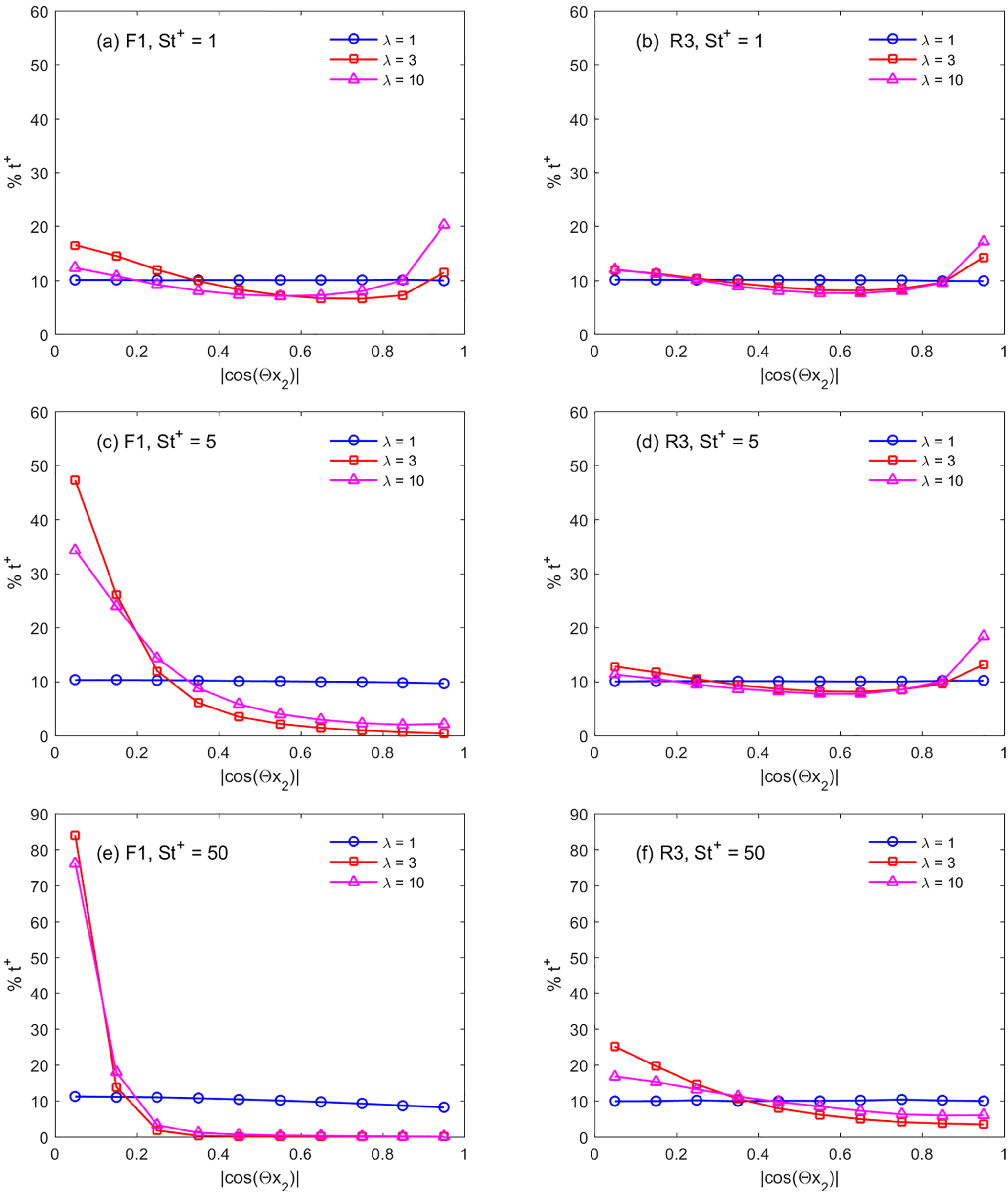

FIG. 12. Spanwise orientation frequency (percent values) in the near-wall region ($x_3^+ < 10$). Panels: (a) Case F1—$\mathrm{St}^+ = 1$, (b) Case R3—$\mathrm{St}^+ = 1$, (c) Case F1—$\mathrm{St}^+ = 5$, (d) Case R3—$\mathrm{St}^+ = 5$, (e) Case F1—$\mathrm{St}^+ = 50$, (f) Case R3—$\mathrm{St}^+ = 50$.

to which the reader is referred for more details. Here, we just recall that particle alignment is classified by subdividing the absolute value of the direction cosines into k equally spaced bins and by computing the overall time $t^+(i, j, k)$ spent by the ith particle belonging to the jth set in the kth bin. The mean time per bin $t^+(j, k)$ is then computed by averaging $t^+(i, j, k)$ over the number of particles per bin, and its percentage value is finally obtained as $\%t^+ = t^+(j, k)/T^+$. Based on this procedure, the orientation frequency spherical particles is always $\%t^+ = 10\%$ (no preferential orientation), as one would expect. Figure 11 shows that elongation always tends to favor particle alignment with the streamwise direction, while the opposite effect is induced by roughness, especially at low inertia. Interestingly, the effect of inertia in the smooth-wall case (left-end panels Fig. 11) is almost negligible up to $\mathrm{St}^+ = 5$ and leads to a reduction of $\%t^+$ for $\mathrm{St}^+ = 50$ and above, shadowing any length effect as can be seen from Fig. 11(e). This latter observation does not hold in the case of rough walls (right-end panels Fig. 11) since length effects can be appreciated also at $\mathrm{St}^+ = 50$, as can be seen from Fig. 11(f). Overall, only quantitative changes can be observed. Looking at the orientation frequency with respect to the spanwise direction, reported in Fig. 12, we find that both roughness and elongation induce rather small changes at low particle inertia, leading to small and *short-lived* deviations from a uniform orientation distribution, as can be appreciated by comparing Figs. 12(a) and 12(b). A remarkable effect of elongation is found in the smooth-wall case for $\mathrm{St}^+ = 5$ and above, as can be seen in Figs. 12(c) and 12(e): Longer fibers tend to align in the plane normal to the spanwise axis, namely in the plane of mean shear where pole-vaulting is more likely to occur. This in particular true in the case of the high-inertia particles, for which values of $\%t^+$ close or above 80% are reached [Fig. 12(e)], a measure of strongly stable orientation state. Again, roughness appears to produce a destabilizing effect that flattens the curves at all Stokes numbers. Interestingly, the largest values of $\%t^+$ are obtained for $\lambda = 3$, indicating a nonmonotonic dependence of the orientation frequency on the aspect ratio that is not found in the streamwise direction. This latter finding, however, is not straightforward to interpret and deserves further analyses to be explained. Overall, Figs. 11 and 12 demonstrate that elongation has in general a stabilizing effect on particle preferential alignment, roughness has a destabilizing effect, whereas inertia favors alignment in the plane of mean shear, albeit not persistently in the streamwise direction: This suggests that, at least in our simulation setting, inertia favors rotation in the plane of mean shear.

IV. CONCLUSIONS

In this work, the dynamics of prolate ellipsoidal particles dispersed in turbulent channel flow bounded by rough walls has been analyzed by means of direct numerical simulation of the turbulence and Lagrangian tracking of the particles. The simulated flow is characterized by a shear Reynolds number $\mathrm{Re}_\tau = 180$ and by dilute flow conditions (which allow to assume a one-way coupling between the two phases). Twelve different particle sets have been considered to examine the effect of particle elongation (parameterized by the particle aspect ratio, $\lambda = 1, 3$, and 10), particle inertia (parameterized by the particle Stokes number, $\mathrm{St}^+ = 1, 5, 50$, and 100), and wall roughness (parameterized by the average absolute deviation of the roughness height, $\bar{k}_s^+ = 0, 2.16, 4.32$, and 9). Hence, a database comprising a total of 48 cases has been considered to perform the study.

Our results show that the spatial distribution of the particles within the flow domain and their translational statistics are weakly affected by the aspect ratio and depend almost exclusively on the combined effect of inertia and wall roughness, which produce large velocity differences in the relative particle-to-fluid velocity throughout the channel: On average, inertial particles tend to lead the fluid in the near-wall region of the channel in the presence of roughness, while lagging the fluid in the bulk of the flow. The lack of length effects can be generally ascribed to turbulence-induced preferential concentration and alignment in the near-wall region, which are observed to occur even with rough walls albeit to a lesser extent. On the one hand, particles tend to sample the same regions of the flow regardless of the aspect ratio and hence interact with similar turbulent structures. On the other hand, particles tend to preferentially align with the wall as they approach it, thus limiting particle-wall interaction. Finite-size effects, which would be observed for particles much thicker and longer than those considered in our study, might change this scenario by triggering local wake dynamics at the particle scale within the flow.

Another effect that can be ascribed to the combined action of inertia and roughness is the occurrence of high wall-normal particle velocities associated with increased particle fluxes to and away from the wall as well as increased mixing. Elongation effects are observed in the particle orientation statistics, which show that longer particles with low inertia exhibit a stronger tendency to align with the mean flow direction. When a particle spends most of its time near the flow direction and hence a shorter time flipping through other orientations, its lift behavior does not resemble that of any equivalent sphere since the fluid velocity disturbance made when the particle is nearly aligned with the flow direction is much smaller than while it is flipping. Roughness is always associated with a destabilizing effect that tends to disrupt preferential alignment, while high inertia favors rotation in the plane of mean shear: This latter orientation state appears to be very persistent in time when particles interact with smooth or nearly smooth walls, but vanishes as wall roughness is increased. Overall, the influence of inertia, elongation and roughness is felt mostly in the near-wall region and much less beyond the buffer layer, regardless of the statistical observable examined.

This study provides a first look into the combined effects of particle inertia, particle elongation and wall roughness on the dynamics of non spherical particles in turbulent channel flow. Further investigation is nonetheless required to confirm from an experimental point of view the dependence of the dispersed phase statistics presented in this study and to extend the analysis to flows at much higher Reynolds numbers, possibly including the effect of fluid inertia, which is known to produce a drift in the particle rotation orbits compared to those predicted by Ref. [38] and simulated here. For instance, the coupling of pole vaulting with the fluid-inertia-induced orientational changes predicted by Ref. [108] may produce a different evolution of the fiber trajectory, moving it away from the wall as shown by Ref. [94] for slender, neutrally buoyant fiber in a wall-bounded shear flow at small Reynolds number.

ACKNOWLEDGMENTS

The authors greatly appreciate the financial support provided by the following projects: RETURN Extended Partnership and received funding from the European Union Next- GenerationEU (National Recovery and Resilience Plan NRRP, Mission 4, Component 2, Investment 1.3 D.D. 1243 2/8/2022, E0000005); TiSento - Sensorialized Composite Pipe for Hydraulic Applications, No. 084221000550 CUP G18I18001710007. Funded under measure 1.1.5 of the PO FESR SICILY 2014-2020; SiciliAn MicronanOTecH Research And Innovation CEnter "SAMOTHRACE" (MUR, PNRR-M4C2, ECS-00000022), spoke 3 - Università degli Studi di Enna "S2-COMMs - Micro and Nanotechnologies for Smart & Sustainable Communities.

[1] F. Lundell, L. D. Söderberg, and P. H. Alfredsson, Fluid mechanics of papermaking, Annu. Rev. Fluid Mech. **43**, 195 (2011).

[2] J. Wang, M. Zhang, L. Feng, H. Yang, Y. Wu, and G. Yue, The behaviors of particle-wall collision for nonspherical particles: Experimental investigation, Powder Technol. **363**, 187 (2020).

[3] F. Jiang, H. Wang, Y. Liu, G. Qi, A. Al-Rawni, P. Nkomazana, and X. Li, Effect of particle collision behavior on heat transfer performance in a down-flow circulating fluidized bed evaporator, Powder Technol. **381**, 55 (2021).

[4] R. Caggiano, S. Sabia, and A. Speranza, Trace elements and human health risks assessment of finer aerosol atmospheric particles (PM1), Environ. Sci. Pollut. Res. **26**, 36423 (2019).

[5] H. Li, Q. Dai, M. Yang, F. Li, X. Liu, M. Zhou, and X. Qian, Heavy metals in submicronic particulate matter (PM1) from a Chinese metropolitan city predicted by machine learning models, Chemosphere **261**, 127571 (2020).

[6] G. Falkovich and A. Pumir, Sling effect in collisions of water droplets in turbulent clouds, J. Atmos. Sci. **64**, 4497 (2007).

[7] K. Gustavsson, M. Z. Sheikh, A. Naso, A. Pumir, and B. Mehlig, Effect of particle inertia on the alignment of small ice crystals in turbulent clouds, J. Atmos. Sci. **78**, 2573 (2021).

[8] P. Burns and E. Meiburg, Sediment-laden fresh water above salt water: Nonlinear simulations, J. Fluid Mech. **762**, 156 (2015).

[9] G. D'Alessandro, Z. Hantsis, C. Marchioli, and U. Piomelli, Accuracy of bed-load transport models in eddy-resolving simulations, Int. J. Multiphase Flow **141**, 103676 (2021).

[10] M. Benedini, Water pollution control, in *Water Resources of Italy*, edited by G. Rossi and M. Benedini World Water Resources, Vol. 5 (Springer, Cham, 2020), pp. 205–229.
[11] R. Chandrappa and D. Das, Air pollution control, *Environmental Health - Theory and Practice* (Springer International Publishing, 2021), Chap. 6, p. 127.
[12] Z. Dodin and T. Elperin, On the collision rate of particles in turbulent flow with gravity, Phys. Fluids **14**, 2921 (2002).
[13] S. Sumbekova, A. Cartellier, A. Aliseda, and M. Bourgoin, Preferential concentration of inertial sub-Kolmogorov particles: The roles of mass loading of particles, Stokes numbers, and Reynolds numbers, Phys. Rev. Fluids **2**, 024302 (2017).
[14] K. O. Fong, O. Amili, and F. Coletti, Velocity and spatial distribution of inertial particles in a turbulent channel flow, J. Fluid Mech. **872**, 367 (2019).
[15] S. Shaik, S. Kuperman, V. Rinsky, and R. van Hout, Measurements of length effects on the dynamics of rigid fibers in a turbulent channel flow, Phys. Rev. Fluids **5**, 114309 (2020).
[16] M. Alipour, M. De Paoli, S. Ghaemi, and A. Soldati, Long nonaxisymmetric fibers in turbulent channel flow, J. Fluid Mech. **916**, A3 (2021).
[17] C. Marchioli and A. Soldati, Mechanisms for particle transfer and segregation in a turbulent boundary layer, J. Fluid Mech. **468**, 283 (2002).
[18] F. Lucci, A. Ferrante, and S. Elghobashi, Modulation of isotropic turbulence by particles of Taylor length-scale size, J. Fluid Mech. **650**, 5 (2010).
[19] S. Balachandar and J. K. Eaton, Turbulent dispersed multiphase flow, Annu. Rev. Fluid Mech. **42**, 111 (2010).
[20] M. Bernardini, Reynolds number scaling of inertial particle statistics in turbulent channel flows, J. Fluid Mech. **758**, R1 (2014).
[21] C. Marchioli, L. Zhao, and H. I. Andersson, On the relative rotational motion between rigid fibers and fluid in turbulent channel flow, Phys. Fluids **28**, 013301 (2016).
[22] G. Wang, K. O. Fong, F. Coletti, J. Capecelatro, and D. H. Richter, Inertial particle velocity and distribution in vertical turbulent channel flow: A numerical and experimental comparison, Int. J. Multiphase Flow **120**, 103105 (2019).
[23] A. Michel and B. Arcen, Reynolds number effect on the concentration and preferential orientation of inertial ellipsoids, Phys. Rev. Fluids **6**, 114305 (2021).
[24] L. Brandt and F. Coletti, Particle-laden turbulence: Progress and perspectives, Annu. Rev. Fluid Mech. **54**, 159 (2022).
[25] J. Lee and C. Lee, Modification of particle-laden near-wall turbulence: Effect of Stokes number, Phys. Fluids **27**, 023303 (2015).
[26] J.-P. Mollicone, M. Sharifi, F. Battista, P. Gualtieri, and C. M. Casciola, Particles in turbulent separated flow over a bump: Effect of the Stokes number and lift force, Phys. Fluids **31**, 103305 (2019).
[27] S. Balachandar, A scaling analysis for point-particle approaches to turbulent multiphase flows, Int. J. Multiphase Flow **35**, 801 (2009).
[28] C. Narayanan, D. Lakehal, L. Botto, and A. Soldati, Mechanisms of particle deposition in a fully developed turbulent open channel flow, Phys. Fluids **15**, 763 (2003).
[29] L. F. Mortimer, D. O. Njobuenwu, and M. Fairweather, Near-wall dynamics of inertial particles in dilute turbulent channel flows, Phys. Fluids **31**, 063302 (2019).
[30] L. Zhao, C. Marchioli, and H. I. Andersson, Stokes number effects on particle slip velocity in wall-bounded turbulence and implications for dispersion models, Phys. Fluids **24**, 021705 (2012).
[31] A. Sozza, M. Cencini, S. Musacchio, and G. Boffetta, Drag enhancement in a dusty Kolmogorov flow, Phys. Rev. Fluids **5**, 094302 (2020).
[32] M. Caporaloni, F. Tampieri, F. Trombetti, and O. Vittori, Transfer of particles in nonisotropic air turbulence, J. Atmos. Sci. **32**, 565 (1975).
[33] M. Reeks, The transport of discrete particles in inhomogeneous turbulence, J. Aerosol Sci. **14**, 729 (1983).
[34] F. Picano, G. Sardina, and C. M. Casciola, Spatial development of particle-laden turbulent pipe flow, Phys. Fluids **21**, 093305 (2009).

[35] G. Voth and A. Soldati, Anisotropic particles in turbulence, Annu. Rev. Fluid Mech. **49**, 249 (2017).

[36] R. Mallier and M. Maxey, The settling of nonspherical particles in a cellular flow field, Phys. Fluids **3**, 1481 (1991).

[37] H. Shin and M. R. Maxey, Chaotic motion of nonspherical particles settling in a cellular flow field, Phys. Rev. E **56**, 5431 (1997).

[38] G. B. Jeffery, The motion of ellipsoidal particles immersed in a viscous fluid, Proc. R. Soc. London A **102**, 161 (1922).

[39] H. Brenner, The Stokes resistance of an arbitrary particle, Chem. Eng. Sci. **18**, 1 (1963).

[40] E. Y. Harper and I.-D. Chang, Maximum dissipation resulting from lift in a slow viscous shear flow, J. Fluid Mech. **33**, 209 (1968).

[41] M. Maxey and J. Riley, Equation of motion for a small rigid sphere in a nonuniform flow, Phys. Fluids, **26** 883 (1983).

[42] F. G. Fan and G. Ahmadi, A Sublayer Model for wall deposition of particles in turbulent streams, J. Aerosol Sci. **26**, 813 (1995).

[43] H. Zhang, G. Ahmadi, F. G. Fan, and J. B. McLaughlin, Ellipsoidal particles transport and deposition in turbulent channel flows, Int. J. Multiphase Flow **27**, 971 (2001).

[44] M. Parsheh, M. Brown, and C. Aidun, On the orientation of stiff fibers suspended in turbulent flow in planar contraction, J. Fluid Mech. **545**, 245 (2005).

[45] G. Sardina, L. Brandt, P. Schlatter, C. M. Casciola, and D. S Henningson, Transport of inertial particles in turbulent boundary layers, J. Phys.: Conf. Ser., **318**, 052020 (2011).

[46] J. Ravnik, C. Marchioli, and A. Soldati, Application limits of Jeffery's theory for elongated particle torques in turbulence: A DNS assessment, Acta Mech. **229**, 827 (2018).

[47] D. Dotto and C. Marchioli, Orientation, distribution, and deformation of inertial flexible fibers in turbulent channel flow, Acta Mech. **230**, 597 (2019).

[48] D. Dotto, A. Soldati, and C. Marchioli, Deformation of flexible fibers in turbulent channel flow, Meccanica **55**, 343 (2019).

[49] P. H. Mortensen, H. I. Andersson, J. J. Gillissen, and B. J. Boersma, Dynamics of prolate ellipsoidal particles in a turbulent channel flow, Phys. Fluids **20**, 093302 (2008).

[50] C. Marchioli, M. Fantoni, and A. Soldati, Orientation, distribution, and deposition of elongated, inertial fibers in turbulent channel flow, Phys. Fluids **22**, 033301 (2010).

[51] L. Zhao, C. Marchioli, and H. I. Andersson, Slip velocity of rigid fibers in turbulent channel flow, Phys. Fluids **26**, 063302 (2014).

[52] F. Zhao and B. G. M. van Wachem, Direct numerical simulation of ellipsoidal particles in turbulent channel flow, Acta Mech. **224**, 2331 (2013).

[53] C. Marchioli and A. Soldati, Rotation statistics of fibers in wall shear turbulence, Acta Mech. **224**, 2311 (2013).

[54] N. R. Challabotla, L. Zhao, and H. I. Andersson, Gravity effects on fiber dynamics in wall turbulence, Flow, Turbul. Combust. **97**, 1095 (2016).

[55] B. Arcen, R. Ouchene, M. Khalij, and A. Tanière, Prolate spheroidal particles' behavior in a vertical wall-bounded turbulent flow, Phys. Fluids **29**, 093301 (2017).

[56] L. Zhao, N. R. Challabotla, H. I. Andersson, and E. A. Variano, Rotation of Nonspherical Particles in Turbulent Channel Flow, Phys. Rev. Lett. **115**, 244501 (2015).

[57] R. Jain and J. Tschisgale, S. abd Fröhlich, Effect of particle shape on bedload sediment transport in case of small particle loading, Meccanica **55**, 299 (2020).

[58] R. Ouchene, J. I. Polanco, I. Vinkovic, and S. Simoëns, Acceleration statistics of prolate spheroidal particles in turbulent channel flow, J. Turbul. **19**, 827 (2018).

[59] F. Sofos, T. Karakasidis, and A. Liakopoulos, Effects of wall roughness on flow in nanochannels, Phys. Rev. E **79**, 026305 (2009).

[60] W. Xu, X. He, X. Hou, Z. Huang, and W. Wang, Influence of wall roughness on cavitation performance of centrifugal pump, J. Brazil. Soc. Mech. Sci. Eng. **43**, 314 (2021).

[61] M. Benson, T. Tanaka, and J. Eaton, Effects of wall roughness on particle velocities in a turbulent channel flow, J. Fluids Eng.—Trans. ASME **127**, 250 (2005).

[62] M. De Marchis and E. Napoli, Effects of irregular two-dimensional and three-dimensional surface roughness in turbulent channel flows, Int. J. Heat Fluid Flow **36**, 7 (2012).
[63] D. Chung, L. Chan, M. MacDonald, N. Hutchins, and A. Ooi, A fast direct numerical simulation method for characterising hydraulic roughness, J. Fluid Mech. **773**, 418 (2015).
[64] M. MacDonald, L. Chan, D. Chung, N. Hutchins, and A. Ooi, Turbulent flow over transitionally rough surfaces with varying roughness densities, J. Fluid Mech. **804**, 130 (2016).
[65] S. Endrikat, D. Modesti, M. MacDonald, R. García-Mayoral, N. Hutchins, and D. Chung, Direct numerical simulations of turbulent flow over various riblet shapes in minimal-span channels, Flow Turbul. Combust. **107**, 1 (2021).
[66] M. De Marchis, B. Milici, and E. Napoli, Numerical observations of turbulence structure modification in channel flow over 2D and 3D rough walls, Int. J. Heat Fluid Flow **56**, 108 (2015).
[67] L. Chan, M. MacDonald, D. Chung, N. Hutchins, and A. Ooi, A systematic investigation of roughness height and wavelength in turbulent pipe flow in the transitionally rough regime, J. Fluid Mech. **771**, 743 (2015).
[68] M. MacDonald, A. Ooi, R. García-Mayoral, N. Hutchins, and D. Chung, Direct numerical simulation of high aspect ratio spanwise-aligned bars, J. Fluid Mech. **843**, 126 (2018).
[69] M. De Marchis, D. Saccone, B. Milici, and E. Napoli, Large eddy simulations of rough turbulent channel flows bounded by irregular roughness: Advances toward a universal roughness correlation, Flow, Turbul. Combust. **105**, 627 (2020).
[70] M. Kadivar, D. Tormey, and G. McGranaghan, A review on turbulent flow over rough surfaces: Fundamentals and theories, Int. J. Thermofluids **10**, 100077 (2021).
[71] E. Napoli, V. Armenio, and M. De Marchis, The effect of the slope of irregularly distributed roughness elements on turbulent wall-bounded flows, J. Fluid Mech. **613**, 385 (2008).
[72] M. De Marchis, E. Napoli, and V. Armenio, Turbulence structures over irregular rough surfaces, J. Turbul. **11**, N3 (2010).
[73] S. Leonardi and I. Castro, Channel flow over large cube roughness: A direct numerical simulation study, J. Fluid Mech. **651**, 519 (2010).
[74] G. Mallouppas and B. van Wachem, Large eddy simulations of turbulent particle-laden channel flow, Int. J. Multiphase Flow **54**, 65 (2013).
[75] B. Milici, M. De Marchis, G. Sardina, and E. Napoli, Effects of roughness on particle dynamics in turbulent channel flows: A DNS analysis, J. Fluid Mech. **739**, 465 (2014).
[76] M. Sommerfeld and J. Kussin, Wall roughness effects on pneumatic conveying of spherical particles in a narrow horizontal channel, Powder Technol. **142**, 180 (2004).
[77] N. Konan, O. Kannengieser, and O. Simonin, Stochastic modeling of the multiple rebound effects for particle–rough wall collisions, Int. J. Multiphase Flow **35**, 933 (2009).
[78] M. Mando and C. Yin, Euler–lagrange simulation of gas–solid pipe flow with smooth and rough wall boundary conditions, Powder Technol. **225**, 32 (2012).
[79] M. De Marchis, B. Milici, and E. Napoli, Solid sediment transport in turbulent channel flow over irregular rough boundaries, Int. J. Heat Fluid Flow **65**, 114 (2017).
[80] B. Milici, M. De Marchis, and E. Napoli, Large eddy simulation of inertial particles dispersion in a turbulent gas-particle channel flow bounded by rough walls, Acta Mech. **231**, 3925 (2020).
[81] K. Luo, Q. Dai, X. Liu, and J. Fan, Effects of wall roughness on particle dynamics in a spatially developing turbulent boundary layer, Int. J. Multiphase Flow **111**, 140 (2019).
[82] L. Chan, T. Zahtila, A. Ooi, and J. Philip, Transport of particles in a turbulent rough-wall pipe flow, J. Fluid Mech. **908**, A1 (2021).
[83] D. Saccone, C. Marchioli, and M. De Marchis, Effect of roughness on elongated particles in turbulent channel flow, Int. J. Multiphase Flow **152**, 104065 (2022).
[84] M. De Marchis and B. Milici, Turbulence modulation by micro-particles in smooth and rough channels, Phys. Fluids **28**, 115101 (2016).
[85] B. Milici and M. De Marchis, Statistics of inertial particle deviation from fluid particle trajectories in horizontal rough wall turbulent channel flow, Int. J. Heat Fluid Flow **60**, 1 (2016).

[86] M. De Marchis, G. Ciraolo, G. Nasello, and E. Napoli, Wind- and tide-induced currents in the stagnone lagoon (sicily), Environ. Fluid Mech. **12**, 81 (2012).
[87] M. De Marchis and E. Napoli, The effect of geometrical parameters on the discharge capacity of meandering compound channels, Adv. Water Resour. **31**, 1662 (2008).
[88] E. Michaelides and Z. Feng, Review—Drag coefficients of nonspherical and irregularly shaped particles, J. Fluids Eng. **145**, 060801 (2023).
[89] M. Zastawny, G. Mallouppas, F. Zhao, and B. van Wachem, Derivation of drag and lift force and torque coefficients for nonspherical particles in flows, Int. J. Multiphase Flow **39**, 227 (2012).
[90] K. Fröhlich, M. Meinke, and W. Schröder, Correlations for inclined prolates based on highly resolved simulations, J. Fluid Mech. **901**, A5 (2020).
[91] S. Tajfirooz, J. G. Meijer, J. G. M. Kuerten, M. Hausmann, J. Fröhlich, and J. C. H. Zeegers, Statistical-learning method for predicting hydrodynamic drag, lift, and pitching torque on spheroidal particles, Phys. Rev. E **103**, 023304 (2021).
[92] A. M. Bhagat and P. S. Goswami, Effect of rough wall on drag, lift, and torque on an ellipsoidal particle in a linear shear flow, Phys. Fluids **34**, 083312 (2022).
[93] A. Zarghami and J. Padding, Drag, lift and torque acting on a two-dimensional nonspherical particle near a wall, Adv. Powder Technol. **29**, 1507 (2018).
[94] J. Dhanasekaran and D. L. Koch, The hydrodynamic lift of a slender, neutrally buoyant fiber in a wall-bounded shear flow at small Reynolds number, J. Fluid Mech. **879**, 121 (2019).
[95] M. Sheikh, K. Gustavsson, D. Lopez, E. Leveque, B. Mehlig, A. Pumir, and A. Naso, Importance of fluid inertia for the orientation of spheroids settling in turbulent flow, J. Fluid Mech. **886**, A9 (2020).
[96] R. Cox, The steady motion of a particle of arbitrary shape at small Reynolds numbers, J. Fluid Mech. **23**, 625 (1965).
[97] R. Khayat and R. Cox, Inertia effects on the motion of long slender bodies, J. Fluid Mech. **209**, 435 (1989).
[98] V. Dabade, N. K. Marath, and G. Subramanian, The effect of inertia on the orientation dynamics of anisotropic particles in simple shear flow, J. Fluid Mech. **791**, 631 (2016).
[99] D. Di Giusto, L. Bergougnoux, C. Marchioli, and E. L. Guazzelli, Influence of inertia on the rotation of axisymmetric particles in shear flow, *Proceedings of the 75th Annual Meeting of the Division of Fluid Dynamics* (APS, College Park, MD, 2022).
[100] M. De Marchis, B. Milici, and E. Napoli, Large eddy simulations on the effect of the irregular roughness shape on turbulent channel flows, Int. J. Heat Fluid Flow **80**, 108494 (2019).
[101] M. De Marchis, B. Milici, G. Sardina, and E. Napoli, Interaction between turbulent structures and particles in roughened channel, Int. J. Multiphase Flow **78**, 117 (2016).
[102] A. Soldati and C. Marchioli, Physics and modeling of turbulent particle deposition and entrainment: Review of a systematic study, Int. J. Multiphase Flow **35**, 827 (2009).
[103] A. Capone, F. Di Felice, and F. Alves Pereira, Flow-particle coupling in a channel flow laden with elongated particles: The role of aspect ratio, J. Mar. Sci. Eng. **9**, 1388 (2021).
[104] M. L. Byron, Y. Tao, I. A. Houghton, and V. E. A., Slip velocity of large low-aspect-ratio cylinders in homogeneous isotropic turbulence, Int. J. Multiphase Flow **121**, 103120 (2019).
[105] L. J. Baker and F. Coletti, Experimental investigation of inertial fibers and disks in a turbulent boundary layer, J. Fluid Mech. **943**, A27 (2022).
[106] G. Sardina, P. Schlatter, L. Brandt, F. Picano, and C. M. Casciola, Wall accumulation and spatial localization in particle-laden wall flows, J. Fluid Mech. **699**, 50 (2012).
[107] P. L. Johnson, M. Bassenne, and P. Moin, Turbophoresis of small inertial particles: Theoretical considerations and application to wall-modeled large-eddy simulations, J. Fluid Mech. **883**, A27 (2020).
[108] G. Subramanian and D. Koch, Inertial effects on fiber motion in simple shear flow, J. Fluid Mech. **535**, 383 (2005).